

For ApJSuppl: final draft — lda, February 10, 2022

The Molecular Properties of Galactic H II Regions

L. D. Anderson¹, T. M. Bania¹, J. M. Jackson¹, D. P. Clemens¹, M. Heyer², R. Simon³, R. Y. Shah⁴, & J. M. Rathborne⁵

ABSTRACT

We derive the molecular properties for a sample of 301 Galactic H II regions including 123 ultra compact (UC), 105 compact, and 73 diffuse nebulae. We analyze all sources within the BU-FCRAO Galactic Ring Survey (GRS) of ¹³CO emission known to be H II regions based upon the presence of radio continuum and cm-wavelength radio recombination line emission. Unlike all previous large area coverage ¹³CO surveys, the GRS is fully sampled in angle and yet covers ~ 75 square degrees of the Inner Galaxy. The angular resolution of the GRS ($46''$) allows us to associate molecular gas with H II regions without ambiguity and to investigate the physical properties of this molecular gas. We find clear CO/H II morphological associations in position and velocity for $\sim 80\%$ of the nebular sample. Compact H II region molecular gas clouds are on average larger than UC clouds: $2'.2$ compared to $1'.7$. Compact and UC H II regions have very similar molecular properties, with ~ 5 K line intensities and $\sim 4 \text{ km s}^{-1}$ line widths. The diffuse H II region molecular gas has lower line intensities, ~ 3 K, and smaller line widths, $\sim 3.5 \text{ km s}^{-1}$. These latter characteristics are similar to those found for quiescent molecular clouds in the GRS. Our sample nebulae thus show evidence for an evolutionary sequence wherein small, dense molecular gas clumps associated with UC H II regions grow into older compact nebulae and finally fragment and dissipate into large, diffuse nebulae.

Subject headings: H II regions — ISM: abundances, clouds, atoms, evolution, lines, and bands, structure — radio lines: ISM

¹Institute for Astrophysical Research, 725 Commonwealth Ave., Boston University, Boston MA 02215, USA.

²Department of Astronomy, University of Massachusetts, Amherst, MA 01003, USA.

³Physikalisches Institut, Universität zu Köln, 50937 Cologne, Germany

⁴MIT Lincoln Laboratory, 244 Wood Street, Lexington, MA 02420

⁵Harvard-Smithsonian Center for Astrophysics, 60 Garden St., Cambridge, MA 02138, USA

1. INTRODUCTION

In the classical view of H II region formation OB stars form inside Giant Molecular Clouds (GMCs). Any newly formed OB star emits extreme ultraviolet (EUV) radiation (> 13.6 eV) and ionizes the surrounding medium of a molecular cloud, creating an H II region. The ionizing photons have more energy than is necessary to ionize the gas, however, and thus some excess energy heats the ambient gas. Because of the pressure difference between the cold, natal molecular cloud (~ 30 K) and the H II region ($\sim 10^4$ K), the ionization front expands into the molecular cloud.

A photodissociation region (PDR) exists beyond the ionization front. The PDR is a zone where photons of energies lower than 13.6 eV ionize elements with low ionization potentials and dissociate molecules (see Hollenbach & Tielens 1997, for a review of dense PDRs). Within the PDR there are three important boundaries. At $A_V \simeq 1$, a dissociation front exists where H_2 replaces H as the dominant species. Further from the emitting star, at $A_V \simeq 4$, there is a boundary between $C^+/C/CO$ where carbon becomes stored predominantly in the CO molecule. The final boundary of the PDR occurs at the O/O_2 transition, $A_V \simeq 10$. The PDR is therefore a transition region between the H II region and the molecular cloud; it is completely ionized at one boundary and completely molecular at the other. Since all H II regions should produce PDRs, in this simplified view all H II regions should have associated molecular gas when they first form. As the nebulae evolve, however, the OB stars can travel far enough to leave the environs of their natal molecular clouds.

Complicating this simple scenario is the fact that molecular clouds are clumpy and inhomogeneous on all scales (e.g., Falgarone & Phillips 1996; Kramer et al. 1998; Simon et al. 2001). In a clumpy medium, EUV photons can penetrate to different depths, creating non-spherical ionization fronts. Additionally, H II regions evolve by moving away from their natal cloud environments and displacing the local gas. Understanding the complicated interaction between young stars, H II regions, and molecular gas is crucial to the study of massive star formation and the impact massive stars have on their environment.

The molecular component of H II regions has been studied in detail by many authors. Most studies, however, have focused mainly on ultra-compact (UC) H II regions (e.g., Churchwell, Walmsley, 1990; Kim & Koo 2003). When compact H II regions were observed in CO, they were often only observed with single pointings using single-dish telescopes (e.g., Brand et al. 1984; Whiteoak, Otrupcek, & Rennie 1982; Russeil & Castets 2004). As our results show, CO gas is frequently offset from the nominal position of an H II region. A completely sampled map is required to understand fully the dynamics and properties of molecular gas associated with H II regions. Furthermore, a sample with H II regions at all evolutionary stages is necessary to understand how this interaction progresses as the H II region ages.

Here we describe a large scale study of the molecular properties of diffuse, compact, and ultra-compact Galactic H II regions using fully sampled CO maps. We trace these molecular properties using the $^{13}\text{CO } J = 1 \rightarrow 0$ emission mapped by the Boston University–Five College Radio Astronomy Observatory (hereafter BU–FCRAO) Galactic Ring Survey (GRS: Jackson et al. 2006). CO is an excellent tracer of molecular material because of its high abundance and the fact that it is rotationally excited at densities common in molecular clouds ($\gtrsim 500 \text{ cm}^{-3}$).

2. Milky Way Surveys

2.1. Galactic H II Regions

Our Galactic H II region source sample is compiled from the H II region radio recombination line (RRL) catalog of Lockman (1989) (hereafter L89), which consists of nearly 500 RRL observations with a $3'$ beam at positions of known continuum emission. These continuum emission sources were drawn from the 5 GHz continuum survey of Altenhoff et al. (1979). All positions in Altenhoff et al. (1979) with a peak flux density greater than 1 Jy beam^{-1} and many sources with peak flux densities down to 0.8 Jy beam^{-1} were observed, unless the source was in a very confused region or was a known supernova remnant (SNR). Since Altenhoff et al. (1979) has coverage from $l = 357.5$ to 60° and $|b| < 1^\circ$, the L89 catalog is complete down to a flux limit of at least 1 Jy at 5 GHz in this region of the Galaxy. This sky coverage entirely overlaps and is much larger than the GRS survey zone (discussed in §2.2), so the L89 catalog is complete at least down to 1 Jy beam^{-1} over the extent of the GRS. The sources in L89 are the classical H II regions first detected in the 1970's at cm-wavelengths using RRLs. Although they are often misidentified, these are not the ultra compact, high density H II regions that are being studied mostly using radio interferometers. Below, to distinguish these classical H II regions from UC nebulae, we will call the L89 nebulae “compact” H II regions.

Our nebular sample also includes diffuse H II regions from Lockman, Pisano, & Howard (1996) (hereafter L96). This catalog consists of RRL measurements at 6 cm ($\sim 6'$ beam) and 9 cm ($\sim 9'$ beam) toward 130 faint, extended continuum sources. Most of these sources are drawn from Altenhoff et al. (1979) and have peak flux densities greater than 0.5 Jy beam^{-1} . The L89 survey is actually the pilot study of this diffuse sample; it contains 40 diffuse sources.

Recently a large catalog of 1442 Galactic H II regions was compiled from 24 published studies of Galactic H II regions (Paladini et al. 2003). These H II regions were found using single-dish, medium resolution (few arcminute beamwidths) observations. For our purposes,

however, this catalog is not useful because nebular positions are given to an accuracy of only 6'.

Finally, our source sample contains UC H II regions taken from Wood & Churchwell (1989a), Kurtz et al. (1994), Watson et al. (2003), and Sewilo, et al. (2004). The Wood & Churchwell (1989a) UC sources were selected by: (1) the presence of a small or unresolved radio source, (2) a spectrum consistent with free-free emission, and (3) strong FIR emission. The UC sources from Kurtz et al. (1994), Watson et al. (2003), and Sewilo, et al. (2004) were selected based on the Wood & Churchwell (1989b) criteria: *IRAS* flux density ratios $\log(F_{25}/F_{12}) \geq 0.57$, $\log(F_{60}/F_{12}) \geq 1.30$, and $F_{100} \geq 1000$ Jy (≥ 700 Jy for Watson et al. (2003)), where F_λ is the *IRAS* flux density at λ μ m.

2.2. The ^{13}CO Galactic Ring Survey

We use the BU-FCRAO ^{13}CO Galactic Ring Survey data¹ (Jackson et al. 2006) to characterize the molecular properties of all H II regions in the GRS. The GRS traces the 5 kpc molecular ring discovered by Burton et al. (1975) and Scoville & Solomon (1975). This annulus of enhanced CO emission dominates the inner Galaxy's structure and harbors most of the Galaxy's star formation regions. The GRS sky coverage spans $18^\circ < l < 55^\circ$ and $|b| < 1^\circ$. Additional, incomplete sky coverage is available for $14^\circ < l < 18^\circ$ over the same latitude range. The GRS covers a total of 74 square degrees. The GRS maps the distribution of emission from the $J = 1 \rightarrow 0$ ($\nu_0 = 110.2$ GHz) rotational transition of ^{13}CO . The ^{13}CO isotopologue is ~ 50 times less abundant than ^{12}CO and hence has a much smaller optical depth. This decreased optical depth yields smaller line widths and gives a cleaner separation of individual velocity components along any specific line of sight compared to previous ^{12}CO surveys.

The GRS, with a spectral resolution of 0.21 km s^{-1} , an angular resolution of $46''$, and a $22''$ angular sampling, improves upon all previous large scale CO surveys. It is the only fully sampled (in solid angle) large scale ^{13}CO survey extant. The GRS improves upon the Bell Labs ^{13}CO survey (Lee et al. 2001) that has a spectral resolution of 0.68 km s^{-1} , an angular resolution of $103''$ and $180''$ angular sampling. The GRS also has better resolution than previous ^{12}CO surveys. For example, the University of Massachusetts Stony Brook survey (Sanders et al. 1986) has a spectral resolution of 1.0 km s^{-1} , an angular resolution of $45''$ and $180''$ angular sampling. The Columbia/CfA ^{12}CO survey (Dame, Hartmann & Thaddeus 2001) has a spectral resolution of 0.18 km s^{-1} , an angular resolution of $450''$ and $225''$ to

¹Data available at <http://www.bu.edu/galacticring/>

450'' angular sampling. Compared to GRS, *all* of these surveys are severely undersampled in angle. The GRS maps have spectra observed at positions separated by $\sim \frac{1}{2}$ the telescope's beamwidth (0.48 HPBW, actually). This, together with high spectral resolution allows us to separate individual ^{13}CO components cleanly. Thus we can for the first time study the molecular properties of Galactic H II regions free from angular sampling bias.

3. H II Region Source Sample

Here we study the molecular properties of all known H II regions in the zone mapped by the GRS. Our sample of 301 H II regions contains 123 UC, 105 compact, and 73 diffuse nebulae. For UC nebulae without RRL measurements in the original papers, we compile RRL velocities from Afflerbach et al. (1996) and Araya et al. (2002) or, if the UC and compact sources were co-spatial, from L89. The compact nebulae are from the L89 catalog. The majority of our diffuse regions are from L96, but a small number are from the pilot survey of diffuse regions in L89. This final nebular sample results from further vetting of the §2 sources using data from several recently completed Galactic scale sky surveys that overlap the GRS zone.

We verify the existence, classification, and position of each H II region by examining the radio continuum and infrared emission at its nominal position. For the radio continuum emission, we primarily use the 21 cm VLA Galactic Plane survey (VGPS: Stil et al. 2006). In addition to the 21 cm H I line emission data cubes, the VGPS generated 21cm continuum images over the range $18^\circ < l < 67^\circ, |b| < 1 - 2$ with $\sim 1'$ resolution. In addition to the VLA measurements, the VGPS used a Green Bank Telescope 21 cm survey to provide the zero spacing data. The VGPS is therefore sensitive to both large and small scale emission. We also use the 20 cm data from the Multi-Array Galactic Plane Imaging Survey (MAGPIS: Helfand et al. 2006). These data were collected with the VLA operating in B-, C-, and D-configurations and have a resolution of $\sim 6''$. The 20 cm MAGPIS data cover the range $5^\circ < l < 48^\circ.5, |b| < 0^\circ.8$. We find MAGPIS to be best suited for verifying UC nebulae, while the VGPS is better suited for verifying compact and diffuse H II regions. For the infrared emission, we use the $8\mu\text{m}$ data from the Galactic Legacy Infrared Mid-Plane Survey Extraordinaire (GLIMPSE: Benjamin et al. 2003) and $24\mu\text{m}$ data from the MIPS Inner Galactic Plane Survey (MIPSGAL: Carey et al. 2008 in preperation). Both infrared surveys have coverage beyond the extent of the GRS.

For inclusion in our sample, we require a continuum peak at the position of each H II region. The UC regions were identified by their IRAS colors and the compact and diffuse regions were located in radio continuum maps with 2'6 resolution. Both of these identification

methods have some level of error that can be reduced through correlation with high resolution radio continuum data. For UC regions, continuum observations are necessary to confirm that the nebula is an H II region, and not a dense protostellar clump. The sources from Wood & Churchwell (1989a) and Kurtz et al. (1994) were confirmed to be UC regions with VLA continuum observations, but the majority of sources from Watson et al. (2003) and Sewilo, et al. (2004) have not yet been confirmed with high resolution radio data. We exclude 11 UC sources, 2 compact sources and 2 diffuse sources that do not have significant continuum emission.

We remove all known SNRs from our sample by comparing our positions with the catalog of Green (2006)² as well as with two recent catalogs of SNRs by Brogan et al. (2006) and Helfand et al. (2006). Both of these recent catalogs compute the spectral index of SNR candidates using 20 cm and 90 cm VLA continuum data and rely on the anticorrelation of SNRs with infrared emission (8 μ m *MSX* data in the case of Brogan et al. (2006) and 21 μ m *MSX* data for Helfand et al. (2006)). We exclude 13 SNRs from our sample that were found in these catalogs, as well as one found in Gaensler, Gotthelf, & Vasisht (1999). There are a comparable number of sources that are spatially coincident with SNRs, but which have a strong IR component. We believe these are H II regions in locations that have produced multiple generations of stars. These sources are retained in our sample. We also remove an additional six sources that do not have infrared emission since they most likely are non-thermal.

Finally, we determine if the classification (UC, compact, diffuse) and position of each source are correct, and remove duplicate sources. We require UC H II regions to have small ($\lesssim 1'$) bright knots of continuum emission, compact regions to be larger bright continuum sources, and diffuse regions to have faint extended continuum emission. There are many cases where an UC region was mistakenly identified as a compact or diffuse region in the L89 and L96 catalogs. This misidentification is due to the fact that UCs are unresolved with the 2.6 beam of Altenhoff et al. (1979) from which L89 and L96 drew their positions. We exclude 69 compact and diffuse nebulae whose positions are coincident with UC regions. Many of the UC H II regions found in the GRS are in large complexes with individual UC components separated by angular distances less than the 46'' GRS beam. We treat these complexes as single UC regions because they share a common molecular gas clump at the GRS resolution.

Table 1 lists the 38 H II regions we cull from our sample because of the criteria just described. Table 1 gives the source name, the reason for exclusion from our sample, and the

²Available at <http://www.mrao.cam.ac.uk/surveys/snrs/>

reference if the source is a known SNR. Source names identify the nebular type: UC (“U”), compact (“C”), or diffuse (“D”). This source name convention will be followed throughout this paper. Figure 1 shows the longitude-velocity position of our nebular sample. The symbols in Figure 1 indicate the nebular type: UC (small filled circles), compact (medium filled circles), or diffuse (large open circles). Table 2 gives the properties of the nebulae in our sample. Listed are the source name, its position in Galactic and equatorial coordinates and its RRL velocity³ with its 1σ error. Altogether our 301 H II region sources probe 266 unique directions since 33 nebulae have RRL emission at several different velocities that presumably originates from physically distinct nebulae located along the line of sight. For some H II regions, we change the classification based on the morphology of the VGPS and MAGPIS radio continuum emission. We also change the position of a few H II regions based on this continuum emission if the position is obviously incorrect. All such changes are noted with footnotes in Table 2.

4. Finding Molecular Gas Associated with Galactic H II Regions

To characterize the properties of molecular gas associated with Galactic H II regions we must establish reliable morphological correlations in (l, b, V) –space between the ^{13}CO gas and the nebulae. The GRS is a large (~ 10 Gbyte), dataset that contains very complex ^{13}CO emission line structure. The (l, b, V_{LSR}) structure of the molecular gas near the nebulae can be very complicated. Any given line of sight frequently contains multiple emission lines. There probably is no single algorithm that can uniquely give reliable CO/H II region (l, b, V) morphological correlations. We therefore use a suite of software tools to analyze the GRS data cubes in a variety of ways.

4.1. Analysis Software

To maximize the power and flexibility of our analysis we wrote a large suite of IDL procedures for spectral analysis rather than use any of the standard single-dish radio astronomy software packages. We used the single-dish radio astronomy TMBIDL⁴ software as our starting point. TMBIDL was originally written to analyze NRAO Green Bank Telescope data.

³The RRL velocities here are in the kinematic Local Standard of Rest (LSR) frame using the radio definition of the Doppler shift. The kinematic LSR is defined by a solar motion of 20.0 km s^{-1} toward $(\alpha, \delta) = (18^{\text{h}}, +30^{\circ})[1900.0]$.

⁴Written by T. M. Bania and available at <http://www.bu.edu/iar/research/dapsdr/>

(TMBIDL was the inspiration that led to the NRAO GBTIDL⁵ software.) The TMBIDL software emulates and improves upon many of the features of the NRAO UniPops analysis program. It includes Gaussian and polynomial line fitting, data visualization, data manipulation, etc. The TMBIDL code can easily be modified to analyze data from any single dish radio telescope.

We wrote additional IDL procedures to interface and analyze GRS data within the TMBIDL environment. TMBIDL was created to analyze single spectra, so we added $(l-V)$, $(b-V)$, and $(l-b)$ mapping tools to better visualize the GRS (l, b, V) data cubes. The basic visualization is a normalized contour map of the CO emission. Using these tools, we found that the morphology of the CO emission at the positions of the H II regions was often very complex.

To gain further control over the visualization of the GRS data, we wrote GUI-based software⁶ to analyze images extracted from the GRS (l, b, V) FITS data cubes. This software provides powerful GUI tools to extract, image, and analyze subcubes for each sample H II region. For our analysis we imaged various quantities for an (l, b) zone surrounding each nebula. The user can, for example, easily modify the velocity channel whose ^{13}CO line intensity is being imaged over the mapped region. One can also quickly create and display integrated intensity CO maps, W_{CO} [K km s^{-1}], as well as arbitrarily vary the velocity range of the integration, ΔV . (This is done with a kernel based algorithm that is fast and efficient.) Sub-images and regions can be created for any image, saved and then reloaded at any time. The GUI uses DS9⁷ syntax to define regions. These regions can have all the basic DS9 shapes. We added a “threshold” region that selects all contiguous pixels above a user-defined threshold level that surround a given image pixel. Using this thresholding tool one can identify and analyze arbitrarily complex morphologies.

This GUI-software is fully integrated with TMBIDL. The user can, for example, export the spectra within any region to TMBIDL for spectral analysis. The ability to scan quickly through velocity channels, create integrated intensity images, select pixels and fit Gaussians to spectra — all within a single application — is extremely powerful.

⁵See <http://gbtidl.sourceforge.net/>

⁶Available for download at <http://people.bu.edu/andersld/>

⁷Available for download at <http://hea-www.harvard.edu/RD/ds9/>

4.2. Correlation of Molecular Gas and H II Regions

Our goal is to find a morphological coincidence in (l, b, V) – space between the CO gas and the H II region. After a coincidence is established, we want to characterize the molecular gas using spectral fits to the ^{13}CO emission. The UC positions are in general known to an accuracy greater than the $22''$ GRS pixel spacing. For the compact and diffuse H II regions, our positions are accurate to a few arcminutes. The RRL LSR velocities are accurate to $\sim 0.1 \text{ km s}^{-1}$ (from Gaussian fits). Although the (l, b, V) position of each nebula is accurately known, establishing a robust set of criteria for identifying a real molecular/H II physical association is nontrivial.

The CO emission maps of H II regions can be quite complex due to GMC structure and PDR/ionization front interactions. For example, one expects the molecular and ionized gas velocities to diverge as an H II region evolves. Once an OB star forms within a GMC its ionization front (IF) expands rapidly at first, reaching the nebular Strömgren radius in $\lesssim 10^5$ yr. The IF pushes the surrounding GMC molecular gas outwards. Dyson & Williams (1997) show that as the IF expands, it rapidly slows until it is expanding at $\sim 10 \text{ km s}^{-1}$ when it reaches the Strömgren radius. Since H II regions are generally older than 10^5 yr (with the possible exception of some UC H II regions), the maximum difference between the RRL and the associated molecular gas should be $\lesssim 10 \text{ km s}^{-1}$.

Our nebular sample has H II regions of different ages and thus should show evolutionary effects. Diffuse H II regions should be older than the UC nebulae, and thus have had more time to evolve away from and displace their natal clouds. The molecular gas in diffuse H II regions should show a weaker association or may not be present at all. We expect the majority of UC and compact H II regions to be associated with a molecular clump (see, e.g., Kim & Koo 2003). Because of these complications, our CO/H II analysis is comprised of a series of distinct investigations.

4.2.1. Single Position Spectrum Analysis

We first examine the GRS ^{13}CO spectrum at the nominal position of each H II region. Most previous studies of the molecular component of H II regions were made using single pointings, e.g., Whiteoak, Otrupcek, & Rennie (1982); Russiel & Castets (2004). All report that the majority of H II regions have associated CO. Whiteoak, Otrupcek, & Rennie (1982) found in their survey of ^{12}CO emission from Southern H II regions that molecular gas within 5 km s^{-1} of the RRL velocity had large line intensities, and therefore was probably associated with the H II region. In their analysis of Southern compact H II regions using both ^{12}CO and

^{13}CO , Russeil & Castets (2004) argued that 10 km s^{-1} is a better criterion for determining a molecular/H II association.

To make a single pointing CO/H II comparison we calculate an average ^{13}CO spectrum at the position of each H II region by convolving the GRS datacube (which is oversampled in angle) with the FCRAO telescope beam (HPBW = $46''$). We then search this average spectrum for a ^{13}CO emission line peak at the H II region RRL velocity. Specifically, we look for emission above 0.5 K brightness temperature, T_{MB} , and within $\pm 2.5 \text{ km s}^{-1}$ of the H II region LSR velocity.

Our brightness temperature limit is chosen to be well above the GRS noise. The GRS data have a typical RMS sensitivity of $\sigma(T_{\text{MB}}) = 0.27 \text{ K}$. The beam convolved average spectrum has a factor of ~ 2 decrease in noise compared to a single GRS position. Thus our 0.5 K search criterion is a $\sim 3\sigma$ limit.

Using the 0.5 K and $\pm 2.5 \text{ km s}^{-1}$ criteria, only 52 % of the nebular sample shows a CO/H II association. Repeating this procedure with the same intensity requirement, but with velocity ranges of $\pm 5.0 \text{ km s}^{-1}$ and $\pm 7.5 \text{ km s}^{-1}$, we find that, respectively, 70% and 79% of H II regions meet these criteria. Certainly increasing the velocity range further still will yield a greater number of nebulae matching the association criteria, but relaxing the association definition in this way also increases the chance of a misidentification and the possibility of blending multiple velocity components.

4.2.2. W_{CO} Integrated Intensity Map Analysis

We use the GRS data to make an (l, b) contour map of the ^{13}CO integrated intensity, W_{CO} (K km s^{-1}), in order to provide information about the spatial distribution of the molecular gas. The main weakness of the single pointing method of searching for CO/H II region associations is that sources with molecular gas offset from the nominal position of the H II region are not counted as detections. For each nebula we use TMBIDL to make normalized W_{CO} contour maps that are $l \times b = 12' \times 12'$ ($\sim 30 \times 30$ GRS pixels) in size. The map W_{CO} is calculated by integrating each spectrum over 15 km s^{-1} centered at the RRL velocity. The map peak W_{CO} is used to normalize the W_{CO} value for each pixel. The final product is a normalized contour map for each nebula in the sample.

We then search each map for W_{CO} peaks and note the distance from the 80% peak W_{CO} contour to the nominal H II region position. We define any source where this distance lies within the H II region positional error bars to be a positive detection and any source where this distance is just outside of the error bars (roughly twice the positional uncertainty) to be

an ambiguous detection. All sources not meeting these positional criteria are deemed to be non-detections. We find that 70% of our sample nebulae show positive detections, 14% have ambiguous detections, and 16% show no correlation between the H II region position and the ^{13}CO emission. Somewhat suprisingly, adding the molecular spatial distribution information to the CO/H II association criterion did not add significantly to the detection rate.

4.2.3. *CO (l, b, V) Data Cube Analysis Procedure*

Clearly, the molecular emission in the GRS is complicated and difficult to characterize. These experiments in establishing a CO/H II region association demonstrate the need for a more sophisticated analysis. We use the §4.1 GUI software to search the GRS ^{13}CO data cubes in (l, b, V) parameter space. For each nebula we make a series of (l, b) W_{CO} images and search for CO/H II region associations. We follow the four step iterative procedure described below and illustrated in Figure 2.

1. We first find the velocity range of the molecular emission associated with the H II region. We examine single velocity channel images (position-position (l, b) maps) centered at the nominal position of the H II region at its RRL velocity with overlaid VGPS 21cm continuum contours. We scan through these single channel images over $\pm 10 \text{ km s}^{-1}$ of the source RRL velocity, searching for the channel where the molecular emission at the position of the H II region has the highest intensity. If we are able to identify a molecular clump near the position of the H II region, we extract the spectra from the voxels near this molecular clump. We fit a Gaussian to the (unweighted) average spectrum of this extracted emission and record the line center and FWHM of the emission line. Frequently, the molecular emission at the H II region position is either absent or has a morphology that is difficult to characterize from single channel maps. For $\sim 25\%$ of our nebulae we are unable to make a molecular gas association from these single channel maps.
2. Next we make an integrated intensity map, W_{CO} , by summing the intensities at a given (l, b) over the range of velocities found in step (1). If the source has an unambiguous CO/H II association, we calculate W_{CO} over the velocity range $V \pm \Delta V/2$, where V is the step (1) Gaussian line velocity and ΔV is its FWHM line width. If the source has an ambiguous step (1) association, we calculate W_{CO} centered at the source RRL velocity over the range $\pm 10 \text{ km s}^{-1}$.
3. We then use the W_{CO} image created in step (2) to find pixels with molecular emission associated with the H II region. We find the brightest emission near the H II region

in the W_{CO} image and select all contiguous pixels that have values above a threshold determined independently for each H II region. The threshold is varied until a small number of pixels are selected — typically 20 to 30. The exact number is set by the molecular clump’s intensity profile. Small clumps with a sharply peaked intensity profile have fewer pixels, whereas larger clumps with a “plateau” of emission have more pixels. This method seeks to isolate single clumps in order to preserve the line peak intensity and minimize blending of multiple velocity components.

4. All the GRS spectra within the (l, b) region selected in step (3) are used to calculate an average ^{13}CO spectrum. We then fit the fewest possible number of Gaussian components to the spectrum in order to maximize the intensity of the peak CO emission. The majority ($\sim 80\%$) of our sources are adequately fit with only one Gaussian component. Many nebulae, however, do not have clean Gaussians profiles, but rather show structure that often suggests a fainter, wider line superposed on a brighter, narrower line.

Our analysis procedure is summarized in Figure 2 for the H II region U43.24–0.05. Panels A and B depict step 1. Panel A shows a single channel GRS map at the velocity nearest the RRL velocity where the molecular clump has the highest intensity. The cross marks the nominal H II region position. For clarity we have not shown the VGPS continuum emission contours. The black box shows the (l, b) positions of the voxels from which we extract spectra to produce the average spectrum shown in Panel B. The vertical line in Panels B and D marks the RRL velocity. Using the velocity range of the emission line shown as dashed lines in Panel B, we create the integrated intensity image shown in Panel C (step 2). This image has been smoothed with a 3×3 Gaussian kernel. The black outline in Panel C shows contiguous integrated intensity values above a threshold (step 3). This region and its threshold is defined by visual inspection of the image. This is the ^{13}CO emission we deem to be associated with the H II region. Finally, we extract the spectra from these (l, b) positions to produce the average spectrum shown in Panel D (step 4). For this source, our method separates the two emission lines that are blended in the panel B spectrum and preserves the peak line intensity.

In principle, we could iterate our analysis to locate and fit the molecular emission more accurately. Using the Panel D Gaussian fit, we could create a new integrated intensity image, define a new CO/H II association region, and fit a Gaussian to this new average spectrum. We did this for 10 test cases and found only minimal changes that were not significantly different from a single pass analysis.

This procedure has many advantages. We are able to characterize the spectral properties of molecular gas distributions that have arbitrary morphologies. We minimize our

assumptions at every stage of the process. By first examining the (l, b) images of each source at individual velocity channels, we limit false detections that may arise from integrated intensity images containing multiple velocity components blended together. By extracting the spectra from regions defined in the integrated intensity images, we make no assumptions based on the visual appearance of the molecular emission at individual velocity channels. By using a variable threshold to select pixels, we are able to characterize molecular structures with arbitrary morphology. This threshold definition ensures clean spectral fitting; the spectra are not contaminated by adjacent pixels that would lower the line intensity and might increase the width of the fitted Gaussian line. Finally, since we analyze an average of many spectra, the lines we fit have a much greater signal to noise ratio than a single pointing spectrum. The Gaussian fit uncertainties in the spectral line parameters we derive are thus minimized.

After we establish a CO/H II region association, we characterize the angular size of the molecular cloud by fitting an ellipse to the W_{CO} spatial distribution. Since the association defined in Panel C of Figure 2 is a W_{CO} threshold value that is determined independently for each source, the size of an ellipse fitted to this zone would have little physical meaning. We therefore define a new threshold selected region that is uniform for the entire nebular sample. This new region is defined by a threshold set to 80% of the W_{CO} peak inside the original association zone. The fitting algorithm calculates the semimajor and semiminor axes using the “mass density” of pixel locations: the clustering of pixel locations along the l and b directions. The fitted ellipse to this region is thus a uniform estimate of the size of the molecular gas associated with the H II region.

The properties we derive for the CO/H II region associations are summarized in Table 3. For each nebula we list the parameters of the ellipse and Gaussian line fits. All errors are 1σ uncertainties. Given are the ellipse centroid in Galactic coordinates, its size, semi-major, a , and semi-minor, b , axes, together with the position angle measured from north toward increasing Galactic longitude. The ellipse size is the geometric mean diameter, $2\sqrt{ab}$. If there are multiple spectral components in the Gaussian fit only the properties of the brightest are listed. We also use only this brightest component in our subsequent analysis. The fitted line parameters given are the center velocity, intensity (in main beam brightness temperature units), and FWHM line width, ΔV . Table 3 also lists some additional nebular properties derived below in §5: the CO excitation temperature, the ^{13}CO column density, and the nebular confidence parameter, CP .

5. Discussion

Our analysis here provides a large sample of molecular cloud/H II region associations whose physical properties are well characterized. In §4 we show that the molecular emission is often morphologically complex and offset from the nominal H II region position and RRL velocity. We find that the traditional single pointing analysis does not reliably detect the molecular components of H II regions. It is very difficult to make a CO/H II association with any confidence without an image produced from a (l, b, V) data cube that spans the entire H II region/PDR/molecular cloud interaction region.

To distinguish sources with an unambiguous molecular gas component at the H II region position and velocity from those with less robust molecular gas associations, we assign a confidence parameter, CP , to each source ranging from A to E. Our qualitative criteria for the confidence parameter are as follows: A: no ambiguity in position or velocity, the molecular gas coincident with radio continuum or shows clear signs of interaction; B: either offset somewhat in position or velocity, or in a complex region of molecular gas; C: either offset in position or velocity or in a complex region, but fainter than a B source and offset further; D: diffuse emission near the correct position and velocity, but uncharacterizable due to low intensity or ambiguous morphology; E: nothing at all apparent in position and velocity.

Figures 3, 4 and 5 give representative examples of our confidence parameter classification. These $20' \times 20'$ ^{13}CO integrated intensity images span the range of molecular gas morphologies surrounding our sample of H II regions. The images are grouped by their confidence parameter classification: Figure 3 shows CP A sources, Figure 4 shows CP B sources and Figure 5 shows CP C, D, and E sources. Because the GRS is oversampled ($22''$ pixels at $46''$ HPBW), we increase the signal to noise by smoothing the images with a 3×3 Gaussian filter.

At the top of each image we list the H II region name, the ^{13}CO line velocity (km s^{-1}) and FWHM line width (km s^{-1}), ΔV , and the source's confidence parameter. These Gaussian fitted line parameters are used to calculate the source's ^{13}CO integrated intensity, $W_{\text{CO}}(\text{K km s}^{-1})$, for the velocity range $V \pm \Delta V/2$. At the bottom of each image we give the W_{CO} calculated from the fitted line: $W_{\text{CO}} = 1.06 T_{\text{MB}} \Delta v$, which is accurate for Gaussian line shapes. Using the procedure described in Simon et al. (2001), we also give an estimate of the H_2 column density, $N(\text{H}_2)[\text{cm}^{-2}]$.

The grey scale image shows the W_{CO} distribution. Normalized contours are drawn at 83%, 67%, 50%, 33% and 16% of this maximum. (One can get quantitative W_{CO} values using the scale bar at the right.) For H II regions where we could not associate molecular gas, the

contour lines are dashed rather than solid and, of course, no line parameters are given.

A bold cross marks the nominal position of the H II region. Plotted in bold is the fitted ellipse described in §4.2.3. If there are other H II regions in the field, they are marked with thinner crosses. The cross arm lengths correspond to the beam size used to make the measurement of the H II region (3' for L89; 9' for L96), except for the UC regions where the cross arm lengths are set to 1'. The GRS beam (HPBW = 46'') is shown in the lower left corner of each image. Shown in grey in these images are VGPS 21cm continuum contours. Tickmarks on these contours point downhill, towards decreasing 21cm emission.

We are able to establish a highly confident (*CP* A and B) CO/H II region association for 62% of the nebulae in our sample. Relaxing the confidence criterion to *CP* A, B and C sources gives CO/H II associations for 84% of our nebular sample. Histograms of the number distribution of confidence parameter values are shown in Figure 6 for UC (open), compact (hatched), and diffuse (gray) nebulae. The top left panel is the stacked histogram of the distribution; the top line represents the entire sample. For example, there are a total of 113 *CP* A sources: 78 UC, 29 compact, and 6 diffuse H II regions. Clockwise from here are the individual histograms for the UC, compact, and diffuse nebulae. (Most subsequent figures will follow this display format.) As is clear from Figure 6, the UC sample has the greatest number of high confidence CO/H II region associations.

Some H II regions appear to have no molecular gas associated with them. Of our 301 sources, 14 (5%) are classified as E sources; these nebulae show no ^{13}CO emission whatsoever. Thirty four sources (11%) are classified as D and therefore have only diffuse emission at the correct position and velocity. Five of our E sources and 15 of our D sources have multiple RRL velocities along the same line of sight. In these cases, one RRL velocity is probably from the H II region of interest while the other is likely from a nearby H II region. Eleven of the 12 UC regions with confidence parameter values of D or E have multiple velocity components.

Two UC H II regions are worth mentioning individually because of the nature of their molecular associations. The UC H II region U33.13+0.09 has a very large velocity offset between the molecular material and the RRL velocity. L89 find a RRL velocity of 93.8 km s^{-1} and Araya et al. (2002) find a RRL velocity of 87.4 km s^{-1} . Our ^{13}CO velocity of 75 km s^{-1} is in agreement with the CS velocity found by Bronfman, Nyman, & May (1996). The morphology and linewidth of the molecular emission suggest that the molecular gas is associated with the H II region. The UC H II region U21.42–0.54 also has a compact molecular clump at the correct (l , b) position. The ^{13}CO velocity of this clump, 54 km s^{-1} , is 16 km s^{-1} offset from its RRL velocity of 70 km s^{-1} . This source was not detected by Bronfman, Nyman, & May (1996). We assign a confidence parameter value of C to

U21.42–0.54 because of the extreme velocity offset.

The lack of CO/H II region associations in $\sim 20\%$ of our sample is not entirely unexpected. This has been reported in the literature before, although previous studies did not have datasets that were fully sampled in angle as is the GRS. Blitz, Fich, & Stark (1982) found a lack of associations in 30% of the Sharpless H II regions studied. Russeil & Castets (2004) found no association with CO in $\sim 20\%$ of their sample of Southern compact H II regions. Churchwell, Walmsley, & Cesaroni (1990) do not detect the dense gas tracer ammonia in $\sim 30\%$ of a sample of 84 UC H II regions.

Our large sample of H II regions contains nebulae spanning a range of evolutionary stages. The UC regions, being young, are more likely to lie within their natal molecular clouds where the density of ^{13}CO should be high. As the H II region evolves, it will dissipate the gas. We should see evidence for this in the compact and diffuse regions. We therefore expect UC regions to be associated with small sizes, high excitation temperatures and column densities, large line widths, and bright line intensities. Diffuse regions should have large sizes and smaller values for the other quantities compared to the UC regions. Compact regions should lie in between these two extremes.

The lack of molecular gas in an H II region can certainly be an evolutionary effect. These nebulae may represent an older population of H II regions that have had time to become displaced from the gas in which they formed due to a variety of mechanisms including, stellar winds, ionization fronts, high stellar space velocities, etc. One observational consequence of this scenario might be a bubble morphology in the molecular gas, seen as a ring in projection. Churchwell et al. (2006) found a large population of bubbles in the GLIMPSE survey (Benjamin et al. 2003). Observed at mid-infrared wavelengths, GLIMPSE boasts an angular resolution 10 times that of the GRS and is therefore a better diagnostic tool for locating bubble features. We indeed see bubbles in ^{13}CO in most H II regions in the GRS for sources where Churchwell et al. (2006) also identified bubbles. These regions are usually classified as D or E sources because the gas has been pushed far away from the center of the continuum emission. Further investigation of this topic will be the subject of a future paper.

5.1. Properties of Molecular Cloud/H II Region Sources

Here we focus on the 253 nebulae with positive CO/H II associations, the subset of our H II region sample with confidence parameter values of A, B or C. The (l, V) distribution of these nebulae is shown in Figure 7 for *CP* A (large filled circles), B (small filled circles), and C (small open circles) sources. Fully 90% of UC and compact nebulae have *CP* A, B, or C

quality CO/H II associations whereas only 64% of the diffuse nebulae do. Diffuse H II regions are probably older on average than either UC or compact nebulae so their significantly lower associate rate with molecular gas provides the first hint of evolutionary effects in our sample.

Table 4 summarizes the mean properties we derive here for this sample. Listed are the mean and standard deviation (1σ) for each quantity. This information is given for the entire sample and also for various subsets of it: UC, compact, and diffuse H II regions as well as sources of *CP* A, B and C. Table 4 lists the number of H II regions in each category, the absolute value of the velocity difference between the ^{13}CO molecular clump and the RRL V_{LSR} , the line intensity (main beam brightness temperature), the FWHM line width, the size of the associated molecular clump, the CO excitation temperature and the ^{13}CO column density.

We estimate the average ^{13}CO column density towards our sources using the Rohlfs & Wilson (1996) analysis:

$$N(^{13}\text{CO})[\text{cm}^{-2}] = 2.42 \times 10^{14} \frac{T_{\text{ex}} \int \tau_{13} dv}{1 - \exp(-5.29) / T_{\text{ex}}} \quad (1)$$

where T_{ex} is the excitation temperature and τ_{13} is the optical depth of the ^{13}CO line. We assume the ^{13}CO emission is optically thin and use the Gaussian fit ^{13}CO line parameters to find the optical depth integral in Eq.1. Both the optical depth and Equation 1, however, depend on the excitation temperature, T_{ex} .

We use the UMSB ^{12}CO $J = 1 \rightarrow 0$ survey (Sanders et al. 1986) to estimate T_{ex} for each source. We assume ^{12}CO is optically thick and use the radiative transfer equation for the $J = 1 \rightarrow 0$ transition to calculate the excitation temperature from the observed main beam brightness temperature, T_{MB}^{12} , of the ^{12}CO line:

$$T_{\text{ex}} = 5.5 \left/ \ln \left(1 + \frac{5.5}{T_{\text{MB}}^{12} + 0.82} \right) \right. . \quad (2)$$

Eq. 2 holds as long as: (1) the ^{12}CO and ^{13}CO emitting gas is in LTE at the same excitation temperature; (2) this gas fills the same volume without clumping; and (3) there are no background continuum sources. (For our nebulae the H II region continuum is subtracted when the spectral baselines are removed.)

For each nebula we first compute an average spectrum from the UMSB survey datacube in exactly the same way as we did for the GRS data. We use the same (l, b) positions from the identical threshold selected region for this average. We then fit Gaussians to these

average spectra. If we fit multiple Gaussians to the GRS data, we attempt to fit the same components to the UMSB data. The spectral resolution of the UMSB survey is 1 km s^{-1} , so this was not always possible as lines resolved in the GRS are blended in the UMSB survey.

Because the pointings of the UMSB survey are further apart than in the GRS ($180''$ compared to $22''$), the UMSB survey underestimates the ^{12}CO emission for the small molecular clumps found in the GRS. For a given velocity, each pixel in the UMSB survey represents ~ 70 pixels in the GRS. Each threshold selected region contains ~ 20 GRS pixels on average, so for the majority of our sources we use only one UMSB pointing to estimate the excitation temperature appropriate for the ^{12}CO emission. Furthermore, this pointing can be as far away as $\sim 120''$ from the GRS position.

The distribution of excitation temperatures we derive is shown in Figure 8. All H II regions in our sample have very similar excitation temperatures near the standard 10 K value assumed for molecular clouds. We expected the excitation temperature of the UC regions in particular to be higher than this standard value as the CO gas is nearer to the exciting star. That we do not see hotter temperatures associated with younger regions is probably due to the effect of the undersampling of the ^{12}CO emission by the UMSB survey. The mean ^{12}CO to ^{13}CO ratio for molecular clumps smaller than the beam spacing of the UMSB survey, $3'$, is ~ 2 while this ratio is ~ 3 for molecular clumps larger than $3'$. Our excitation temperatures, and hence column densities, are therefore lower limits. Because of their small size, UCs are affected more by the difference in sampling between the GRS and the UMSB survey. The UCs also suffer from beam dilution which will lower the inferred excitation temperature.

Nevertheless, we use these excitation temperatures to compute the ^{13}CO column density for each source using Eq. 1. These column densities are listed in Table 2. We then estimate the H_2 column density,

$$N(\text{H}_2) = \left[\frac{^{12}\text{CO}}{^{13}\text{CO}} \right] \times \left[\frac{\text{H}_2}{^{12}\text{CO}} \right] \times N(^{13}\text{CO}), \quad (3)$$

by assuming constant values for these abundance ratios. Following Simon et al. (2001) we adopt a $^{12}\text{CO}/^{13}\text{CO}$ ratio of 45 and a $\text{H}_2/^{12}\text{CO}$ ratio of 8×10^{-5} . Our ^{13}CO and H_2 column density results are summarized in Figure 9. As expected, the UC nebulae have on average the highest column densities and the diffuse nebulae the lowest. Too, the *CP A* sources have on average over twice the column density of the *CP C* nebulae.

We find that the CO gas has on average only a small velocity offset from the H II region RRL velocity. Figure 10 shows the difference between the velocity of the CO gas and the

RRL velocity. There is no difference in velocity offset between the various types of H II regions. The Gaussian fit to the entire distribution is centered at 0.4 km s^{-1} with a FWHM of 8.5 km s^{-1} , whereas the mean of the distribution is $0.2 \pm 3.8 \text{ km s}^{-1}$. The fact that the distribution is centered at zero velocity offset is to be expected for a RRL selected sample of H II regions and an optically thin tracer such as ^{13}CO .

This result is in contrast to optically selected samples where a positive velocity offset was found (e.g., Fich, Dahl, & Treffers 1990). Optical samples choose specific CO/H II region line of sight geometries. Face-on or edge-on blister sources such as the Orion nebula and M17 should dominate these samples. In our sample there is no preferred radial location for H II regions within molecular clouds. Because we do not know the CO/H II geometry with respect to the line of sight, the absolute value of the CO/RRL velocity difference will be a direct measure of any systematic velocity offset between the molecular and ionized gas. Table 4 therefore lists the mean absolute value of the CO/RRL velocity difference; it shows that there is a $\sim 3 \text{ km s}^{-1}$ average flow velocity between the molecular and ionized gas for the nebulae in our sample. This value is independent of the type of H II region, but increases slightly as the *CP* value decreases from A to C.

Figure 11 shows the distribution of ^{13}CO line intensities for our sample. Based on the evolutionary model of H II regions the natal cloud is gradually dissipated by photo-dissociation, photo-ionization, and expanding motions. We expect the ^{13}CO density to decrease as the region progresses from UC to compact and then, finally to diffuse. Assuming ^{13}CO is optically thin, or at least marginally so, the higher densities found in UC regions would lead to higher line intensities, whereas compact sources should show lower line intensities, and diffuse sources the lowest. This hypothesis is only partially borne out as UC and compact regions share the same distribution, averaging $5.21 \pm 0.23 \text{ K}$ and $4.96 \pm 0.24 \text{ K}$, respectively. Diffuse regions do show lower line intensities of 3.32 ± 0.19 . The errors quoted here are the standard errors of the mean, $\text{s.e.m.} \equiv \sigma/\sqrt{N}$.

Figure 12 shows the distribution of ^{13}CO line widths for our sample. The Gaussian fit to this distribution is centered at 4.0 km s^{-1} with a FWHM of 3.2 km s^{-1} . The mean of this distribution is $4.20 \pm 0.09 \text{ km s}^{-1}$. We expected UC H II regions to have significantly broader lines than compact H II regions because the molecular gas is closer to the exciting star and the outflows should be stronger. Once again, this is not the case: the UC and compact distributions are very similar, averaging $4.43 \pm 0.13 \text{ km s}^{-1}$ (s.e.m) and $4.23 \pm 0.14 \text{ km s}^{-1}$ (s.e.m.), respectively. UC and compact regions do have broader lines than the diffuse regions which average $3.56 \pm 0.20 \text{ km s}^{-1}$ (s.e.m.). This suggests that the central star(s) may no longer be significantly heating molecular gas near diffuse H II regions.

This distribution of line widths is comparable to that found by Russeil & Castets (2004)

in their single pointing survey of southern H II regions. They find that the $^{13}\text{CO } J = 1 \rightarrow 0$ line has an average line width of 3.7 km s^{-1} with a standard deviation of 1.9 km s^{-1} . In a study of UC H II regions, Kim & Koo (2003) find an average line width of 6.8 km s^{-1} in the $^{13}\text{CO } J = 1 \rightarrow 0$ transition. Their calculation of line width, however, was based on the average spectrum over the entire map area, which was as large as $30' \times 40'$. For the 8 UC regions in our sample that Kim & Koo (2003) study, we measure a line width of 5.0 km s^{-1} whereas they measure 7.2 km s^{-1} . Using the same large areas to compute the line widths for these sources, we find an average line width of 7.3 km s^{-1} .

The angular size distribution of the H II CO sources is shown in Figure 13. These sizes are defined as the geometric mean of the major ($2 \times a$) and minor ($2 \times b$) axes of the fitted ellipse, $2\sqrt{ab}$. (See §4.2.1 for our ellipse fitting procedure.) There are 6 sources that have sizes greater than $10'$ that are not plotted in Figure 13. These sources are invariably clumps in a large region of extended molecular emission, which makes our method of determining the angular size unreliable.

The molecular clumps associated with UC regions do show the smallest sizes, as expected, averaging 1.7 ± 0.1 (s.e.m.). Compact H II regions are slightly larger, averaging 2.2 ± 0.1 (s.e.m.). The average size of the molecular gas associated with diffuse H II regions lies in between that of UC and compact H II regions, averaging 1.9 ± 0.1 (s.e.m.). We have removed the 6 sources with sizes greater than $10'$ from the statistical analysis. The molecular gas around many diffuse regions is fragmented, which leads to the small angular sizes we measure. Since we only associate a single molecular clump of contiguous pixels with each nebula, for diffuse H II regions we probably have not characterized all the associated molecular gas.

5.2. Comparison with GRS Molecular Clumps

The properties of molecular clumps in the GRS were analyzed down to size scales of $\sim 1'$ (Rathborne et al. 2008, in preparation). The contiguous pixel finding algorithm *CLUMPFIND* (Williams, de Geus, & Blitz 1994) was used to locate Giant Molecular Clouds (GMCs) within the GRS. Then, by altering the size threshold in *CLUMPFIND*, the clumps within the GMCs were identified and characterized. The distribution of peak intensities and line widths for these clumps shows a Gaussian core with an exponential tail at high values of each parameter. The break points where the distributions turn over from being dominated by the Gaussian core to being dominated by the exponential tail are roughly 4 K and 2 km s^{-1} . By number the vast majority of these GRS molecular clumps have line intensities below 4 K and line widths below 2 km s^{-1} .

The molecular gas associated with H II regions has on average a greater line intensity and larger line width compared to molecular clumps in the GRS. We plot in Figure 14 the line intensity versus the FWHM line width for the molecular clumps associated with our H II regions: UC (filled triangles), Compact (filled circles), and Diffuse (open squares) nebulae. The solid lines divide the plot into quadrants according to the break points of the GRS clumps. A similar plot was used by Clemens & Barvainis (1988) to show that the small clouds in their optically selected molecular cloud sample were cool and quiescent.

The lower left quadrant in Figure 14 should be populated by cold quiescent clouds. These objects are neither making stars nor being externally heated. The upper left quadrant should contain a population of clumps that are heated externally. These clouds are warm (or have high column densities), but do not have the non-thermal motions that would be present if they possessed a central star. The upper right quadrant should contain molecular gas associated with embedded massive stars. The lower right quadrant should contain embedded protostars. These large line width objects are likely active sites of star formation, or near an active site. Thus the lower, < 4 K, part of the plot has a pre-stellar population whereas the upper part contains clouds that are affected by local massive stars.

The UC and compact nebulae occupy the same region of Figure 14; they have similar molecular properties. The diffuse regions, however, have lower line intensities and line widths; they are similar to the general population of molecular clumps. These clumps are no longer being heated significantly by the ionizing star.

Most of our sources with associated ^{13}CO , 54%, lie in the upper right quadrant of Figure 14 where large line intensities and broad line widths suggest active star formation. The vast majority of GRS clumps, as well as most of the molecular clouds in Clemens & Barvainis (1988), reside in the lower left quadrant. The bulk of our remaining nebulae, 42%, lie in the lower right quadrant. The UC, compact, and diffuse regions all have a significant population in this quadrant. It is tempting to think that these low line intensities are due to the decreased optical depth of ^{13}CO but Figure 14 looks very similar to the same plot in Russeil & Castets (2004) made using the optically thick ^{12}CO $J = 2 \rightarrow 1$ transition.

5.3. Are Molecular Cloud/H II Region Associations Real?

Are these CO/H II region associations really sources that are having a direct physical interaction between the H II region and ambient molecular gas? The associations are based on morphological matches in position and velocity between the ^{13}CO gas, RRL velocity, and radio continuum emission. But correlation does not imply causality: these matches could in

principle be a coincidental juxtaposition projected on the sky into the same solid angle by molecular clouds and H II regions located at entirely different places along the line of sight.

That we require a morphological match in (l, b, V) – space places a severe constraint on a false positive association. Mere (l, b) coincidence is not enough; the velocity also needs to match. The kinematic distance ambiguity in the Inner Galaxy makes it possible for the H II region and CO cloud to be at different line of sight positions despite having nearly identical radial velocities. But these are special places because only they share the same LSR velocity. Assessing the quantitative probability of a false positive association is beyond the scope of this paper. To our knowledge no one has yet done the detailed modelling this would require. One needs to know the Galactic distribution of the clouds which posits a detailed knowledge of Galactic structure. For a false positive association we require that there not be a cloud at the H II region position, but that there be a cloud at the other kinematic distance. One thus needs to evaluate separately for each H II region the line of sight distance derivative of the LSR velocity, dV/dr in order to assess the path lengths at the near and far kinematic distances that must be populated. This requires a detailed knowledge of Galactic kinematics, including streaming motions caused by spiral arms. With this information one might be able to estimate the probability of a false positive association. We probably do not know enough about either Galactic structure or Galactic kinematics to do this.

The fact, however, that $\sim 20\%$ of the H II regions do not have associated CO gas (§5.1) is evidence that suggests chance line of sight superpositions in (l, b, V) – space are rare. Furthermore, Figure 14 provides strong support for the physical reality of our CO/H II region associations. Our ^{13}CO clouds are not only near to the H II regions in (l, b, V) – space, but their spectra also have the trademarks of star formation: bright lines and large line widths. This is in marked contrast to the spectral line properties of the vast majority of GRS clouds (see §5.2). Only 1/3 of the GRS clumps have peak intensities $> 4\text{ K}$ whereas 55% of our CO/H II associated clouds do. Only 1/6 of the GRS clouds have line widths $> 2\text{ km s}^{-1}$; nearly all of our clouds, 96%, exceed this value. We conclude that most of the CO/H II region associations must be nebulae with real physical interactions between the molecular and ionized gas.

6. The GRS H II Region Catalog

Our analysis here produced a catalog of Figure 3 type images and physical properties for the sample of 301 Galactic H II regions. We created a website⁸ to give everyone access

⁸http://www.bu.edu/iar/hii_regions

to this information. In addition to the images of nebular W_{CO} , this website has the average ^{13}CO spectrum of each source as well as all the information found in Tables 2 and 3. We expect this website to be an evolving database compiling additional information about these nebulae as it becomes available.

7. Future Work

Our sample of CO/H II region associations will enable many further studies of the properties of star forming regions at all stages of their evolution. The most important parameter that is missing here is the distance to each nebula. Knowing the distance would enable us to derive the intrinsic physical properties of each nebula, establishing their physical sizes and turning column densities and line intensities into masses and luminosities.

Anderson & Bania (2008)[AB hereafter] use H I absorption studies to derive kinematic distances toward all the H II regions with associated molecular gas. All our nebulae are in the first Galactic quadrant, so their distances are degenerate due to the kinematic distance ambiguity. Using the fact that H I absorbs thermal continuum from the H II region, AB use the VGPS 21cm H I emission line maps to remove this degeneracy (see Kuchar & Bania 1994). This is a proven technique as there is sufficient residual cold H I associated with almost all GRS molecular clouds to produce significant absorption (Jackson et al. 2002; Kolpak et al. 2003; Flynn et al. 2004). We shall then use these distances to analyze this nebular sample and derive the physical properties of the dust and gas (ionized, atomic & molecular). The completion of the *Spitzer* GLIMPSE (Benjamin et al. 2003) and MIPS GAL (Carey et al. 2008 in preparation) surveys, together with the GRS (Jackson et al. 2006), MAGPIS (Helfand et al. 2006), NVSS (Condon et al. 1998) and the VGPS surveys enable for the first time a multi-wavelength analysis of the physical properties and evolutionary state of a large sample of inner Galaxy H II regions. Due to our large sample size, we will be able to find examples of H II regions at all evolutionary stages.

8. Summary

We analyzed the GRS ^{13}CO molecular gas associated with all known H II regions covered by the GRS using multiple analysis techniques. Our sample includes 301 regions: 123 UC, 105 compact and 73 diffuse H II regions. We found that 80% of our H II regions showed positive molecular associations, with UCs having the highest association percentage and diffuse regions the lowest. About 5% of our sample showed no molecular emission whatsoever. We

hypothesize that some of these non-detections represent an older population of H II regions where the molecular gas has been displaced from the central star or stars. We found that the molecular properties of UC and compact H II regions are quite similar, with line widths averaging $\sim 4 \text{ km s}^{-1}$ and ^{13}CO column densities of about $3.5 \times 10^{16} \text{ cm}^{-2}$. The molecular gas associated with diffuse regions has properties more consistent with quiescent clouds. The molecular gas properties of our sample nebulae are consistent with an evolutionary sequence wherein small, dense molecular gas clumps associated with UC H II regions grow into older compact nebulae and finally fragment and dissipate into large, diffuse nebulae.

This publication makes use of molecular line data from the Boston University-FCRAO Galactic Ring Survey (GRS). The GRS is a joint project of Boston University and Five College Radio Astronomy Observatory, funded by the National Science Foundation under grants AST-9800334, AST-0098562, & AST-0100793. The National Radio Astronomy Observatory is a facility of the National Science Foundation operated under cooperative agreement by Associated Universities, Inc.

REFERENCES

- Altenhoff, W.J., Downes, D., Pauls, T., & Schraml, J. 1979, *A&AS*, 35, 23
- Afflerbach, A., Churchwell, E., Accord, J.M., Hofner, P., Kurtz, S., & DePree, C.G. 1996, *ApJS*, 106, 423
- Anderson, L.D. & Bania, T.M. 2008, *ApJ*, submitted
- Araya, E., Hofner, P., Churchwell, E., & Kurtz, S. 2002, *ApJS*, 138, 63
- Benjamin, R. A., et al. 2003, *PASP*, 115, 953
- Blitz, L., Fich, M., & Stark, A.A. 1982, *ApJS*, 49, 183
- Brand, J., van der Bij, M.D.P., de Vries, C.P., Leene, A., Habing, H.J., Israel, F.P., de Graauw, T., van de Stadt, H., & Wouterloot, J.G.A. 1984, *A&A*, 139, 181
- Brand, J. 1986, PhD Thesis, Leiden Univ. (Netherlands)
- Brogan, C. L., Gelfand, J. D., Gaensler, B. M., Kassim, N. E., & Lazio, T. J, 2006, */apj*, 639, 25
- Bronfman, L., Nyman, L-A. & May, J. 1996, *A&AS*, 115, 81

- Burton, W. B., Gordon, M.A., Bania, T.M., & Lockman, F.J. 1975, ApJ, 202, 30
- Churchwell, E., Walmsley, C.M., & Cesaroni, R. 1990, A&AS, 83, 119
- Churchwell, E., et al. 2006, ApJ, 649, 759
- Clemens, D. P. 1985, ApJ, 295, 422
- Clemens, D. P. & Barvainis, R. 1988, ApJS, 68, 257
- Clark, J. S., Egan M. P., Crowther P. A., Mizuno D. R., Larionov V. M., & Arkharov A. 2003, A&A, 412, 185
- Condon, J. J., Cotton, W. D., Greisen, E. W., Yin, Q. F., Perley, R. A., Taylor, G. B., & Broderick, J. J. 1998, AJ, 115, 1693
- Dame, T. M., Hartmann, D., & Thaddeus, P. 2001, ApJ, 547, 792
- Dyson, J. E., & Williams, D. A. 1997, The Physics of the Interstellar Medium (2nd ed.; Bristol: Inst. Physics)
- Falgarone E. & Phillips, T.G. 1996, ApJ, 472, 191
- Fich, L., Dahl, G., & Treffers, R. 1990, AJ, 99, 622
- Flynn, E. S., Jackson, J. M., Simon, R., Shah, R. U., Bania, T. M. & Wolfire, M. 2004, ASP Conference Series, 317, 44
- Gaensler, B. M., Gotthelf, E. V., & Vasisht, G. 1999, ApJ, 526, 37
- Green, D.A. 2006, A Catalog of Galactic Supernova Remnants (2006 April version), Mullard Radio Astronomy Observatory, Cavendish Laboratory (Cambridge, United Kingdom)
- Helfand, D.J., Becker, R.H., White, R.L., Fallon, A., and Tuttle, S. 2006, AJ, 131, 2525
- Hollenbach, D. J., & Tielens, A. G. G. M. 1997, ARA&A, 35, 179
- Jackson, J. M., Bania, T. M., Simon, R., Kolpak, M., Clemens, D. P. & Heyer, M. 2002, ApJ, 566, 81
- Jackson, J. M., Rathborne, J.M., Shah, R.Y., Simon, R., Bania, T.M., Clemens, D.P., Chambers, E.T., Johnson, A.M., Dormody, M. & Lavoie, R. 2006, ApJS, 163, 145
- Kim, K. & Koo, B. 2003, ApJ, 596, 362

- Kolpak, M.A., Jackson, J.M., Bania, T.M., & Clemens, D.P. 2003, *ApJ*, 582, 756
- Kramer, C., Stutzki, J., Röhrig, R., & Corneliussen, U. 1998, *A&A*, 329, 249
- Kuchar, T.A. & Bania, T.M. 1994, *ApJ*, 436, 117
- Kurtz, S., Churchwell, E., Wood, D.O.S. & Myers, P. 1994, *ApJS*, 91, 659
- Kwok, S., Volk, K., & Bidelman W.P. *ApJS*, 1997, 112, 557
- Lee, Y., Stark, A. A., Kim, H., & Moon, D. 2001, *ApJS*, 136, 137
- Lockman, F. J. 1989, *ApJS*, 71, 469
- Lockman, F. J., Pisano, D. J., & Howard, G. J., *ApJ*, 472, 173
- Paladini R., Burigana C., Davies R. D., Maino D., Bersanelli M., Cappellini B., Platania P., & Smoot G. 2003, *A&A*, 397, 213
- Rohlfs, K. & Wilson, T.L. 1996, *Tools of Radio Astronomy*, (3rd ed.; Heidelberg: Springer)
- Russek, D. & Castets, A. 2004, *A&A*, 417, 107
- Sanders, D.B., Clemens, D.P., Scoville, N.Z., & Solomon, P.M. 1986, *ApJS*, 60, 1
- Scoville, N. Z. & Solomon, P. M. 1975, *ApJ*, 199, L105
- Simon, R., Jackson, J.M., Clemens, D.P., & Bania, T.M. 2001, *ApJ*, 551, 747
- Sewilo, M., Churchwell, E., Kurtz, S., Goss, W.M., Hofner, P. 2004, *ApJ*, 605, 285
- Stephenson, C.B. 1992, *AJ*, 103, 263
- Stil, J. M., et al. 2006, *AJ*, 132, 1158
- Watson, C., Araya, E., Sewilo, M., Churchwell, E., Hofner, P., & Kurtz, S. 2003, *ApJ*, 587, 714
- Whiteoak, J. B., Otrupcek, R. E., & Rennie, C. J. 1982, *PASAu*, 4, 434
- Williams, J.P., de Geus, E. J., & Blitz, L. 1994, *ApJ*, 428, 693
- Wood, D.O.S. & Churchwell, E. 1989, *ApJ*, 69, 831
- Wood, D.O.S. & Churchwell, E. 1989, *ApJ*, 340, 265

Table 1. Faux and Anomalous Sources

Source	Notes	Reference
C14.32+0.13	SNR	a
D15.45+0.19	SNR	a
D15.52−0.14	SNR	b
U16.58−0.05	No continuum peak	
D17.23+0.39	Probably an evolved star	c, d
U17.64+0.15	No continuum peak	
C18.64−0.29	SNR	a, e
U19.12−0.34	No continuum peak	
U19.36−0.02	No continuum peak	
C19.88−0.53	No continuum peak	
C20.26−0.89	No IR	
C20.48+0.17	SNR	a, e
D21.56−0.11	SNR	a, e
D22.04+0.05	No continuum peak	
D22.16−0.16	Star	c
D22.40−0.37	SNR	e
C22.94−0.07	No IR	
C23.07−0.37	No IR - Part of SNR?	
C23.07−0.25	No IR - Part of SNR?	
D23.16+0.02	No continuum peak	
U23.24−0.24	No continuum peak	
D26.47+0.02	WR or LBV	f
U26.51+0.28	No continuum peak	
C27.13−0.00	SNR	e
C29.09−0.71	SNR	e
D29.55+0.11	SNR	g
U30.42+0.46	No continuum peak	
D30.69−0.63	No IR	
U30.82+0.27	No continuum peak	
C30.85+0.13	SNR	e
C31.05+0.48	SNR	e
D31.61+0.33	SNR	e
D31.82−0.12	SNR	e
U33.24+0.01	No continuum peak	
C45.48+0.18	No continuum peak	
U49.67−0.45	No continuum peak	
C50.23+0.33	No IR	
U53.63+0.02	No continuum peak	

^aBrogan et al. (2006)

^bBrogan et al. (2006) (low confidence detection)

^cStephenson (1992)

^dKwok, Volk, & Bidelman (1997)

^eHelfand et al. (2006)

^fClark et al. (2003)

⁸Gaensler, Gotthelf, & Vasisht (1999)

Table 2. H II Region Source Sample

Source	l (°)	b (°)	RA(2000.0) (h m s)	DEC(2000.0) (° ' ")	V_{LSR} (km s ⁻¹)	Reference	Comments
D15.00+0.05a	15.00	+0.05	18 17 41	−15 52 50	26.5 ± 1.6	L96	
D15.00+0.05b	63.5 ± 1.7	L96	
D15.64−0.24	15.64	−0.24	18 19 60	−15 27 10	61.8 ± 1.3	L96	
C16.31−0.16	16.31	−0.16	18 21 01	−14 49 30	49.5 ± 0.7	L89	
C16.43−0.20	16.43	−0.20	18 21 24	−14 44 10	44.5 ± 0.9	L89	
D16.61−0.32	16.61	−0.32	18 22 11	−14 38 10	44.9 ± 0.6	L89	a
D16.89+0.13	16.89	+0.13	18 21 05	−14 10 30	42.3 ± 1.6	L96	
D17.25−0.20a	17.25	−0.20	18 22 59	−14 00 50	49.9 ± 1.4	L96	
D17.25−0.20b	96.5 ± 1.9	L96	
U18.15−0.28	18.15	−0.28	18 25 01	−13 15 20	53.9 ± 0.4	L89	

^aChanged nebular classification from compact

Note. — Table 2 is published in its entirety in the electronic edition of the Astrophysical Journal Supplement Series. A portion is shown here for guidance regarding its form and content.

Table 3. Properties of Molecular Cloud/H II Region Sources

Source	Fitted Ellipse Parameters					Fitted Gaussian Parameters			T_{ex} K	$N(^{13}\text{CO})$ ($\times 10^{16} \text{ cm}^{-2}$)	CP
	l ($^{\circ}$)	b ($^{\circ}$)	Size ($'$)	Maj. \times Min. ($' \times '$)	PA ($^{\circ}$)	V (km s^{-1})	T_{MB} (K)	ΔV (km s^{-1})			
D15.00+0.05a	14.93	+0.02	2.1	1.6×0.7	+88.6	25.85 ± 0.02	6.03 ± 0.02	3.77 ± 0.05	12.7	3.2	B
D15.00+0.05b	E
D15.64−0.24	15.66	−0.21	2.0	2.1×0.5	+70.6	56.96 ± 0.06	1.88 ± 0.06	1.86 ± 0.09	8.6	0.4	B
C16.31−0.16	16.36	−0.21	1.7	0.9×0.8	+45.0	47.56 ± 0.11	4.17 ± 0.11	4.68 ± 0.12	11.0	2.6	B
C16.43−0.20	16.36	−0.21	1.7	0.9×0.8	+14.9	48.83 ± 0.02	9.47 ± 0.02	2.74 ± 0.04	13.9	3.9	B
D16.61−0.32	16.56	−0.34	4.8	2.9×2.0	+26.3	43.23 ± 0.01	5.39 ± 0.01	4.44 ± 0.04	11.1	3.2	C
D16.89+0.13	D
D17.25−0.20a	17.23	−0.24	3.9	2.7×1.4	−63.4	44.57 ± 0.03	5.62 ± 0.03	4.05 ± 0.07	15.7	3.6	B
D17.25−0.20b	D
U18.15−0.28	18.15	−0.31	2.2	1.7×0.7	+77.9	52.53 ± 0.04	7.32 ± 0.04	4.75 ± 0.06	24.6	7.6	A

Note. — Table 3 is published in its entirety in the electronic edition of the Astrophysical Journal Supplement Series. A portion is shown here for guidance regarding its form and content.

Table 4. Mean Properties of Nebulae with Associated ^{13}CO

	N	$ V $ Offset (km s^{-1})	T_{MB} (K)	ΔV (km s^{-1})	Size ($'$)	T_{ex} (K)	$N(^{13}\text{CO})$ ($\times 10^{16} \text{ cm}^{-2}$)
All	253	2.98 ± 2.41	4.77 ± 2.32	4.19 ± 1.42	1.9 ± 1.3	12.1 ± 4.8	3.1 ± 2.6
UC	111	3.03 ± 2.61	5.21 ± 2.40	4.43 ± 1.38	1.7 ± 1.1	12.2 ± 5.0	3.5 ± 2.8
Compact	95	3.01 ± 2.37	4.96 ± 2.36	4.23 ± 1.40	2.2 ± 1.6	13.3 ± 4.7	3.3 ± 2.6
Diffuse	47	2.81 ± 2.01	3.32 ± 1.29	3.56 ± 1.37	1.9 ± 1.0	9.3 ± 3.0	1.6 ± 1.0
A	112	2.65 ± 2.06	5.63 ± 2.51	4.52 ± 1.26	1.7 ± 0.8	12.8 ± 5.1	4.0 ± 3.0
B	75	3.00 ± 2.37	4.62 ± 2.06	4.05 ± 1.31	2.1 ± 1.5	12.1 ± 4.4	2.8 ± 2.0
C	66	3.53 ± 2.90	3.46 ± 1.51	3.80 ± 1.66	2.2 ± 1.7	11.0 ± 4.4	1.9 ± 1.9

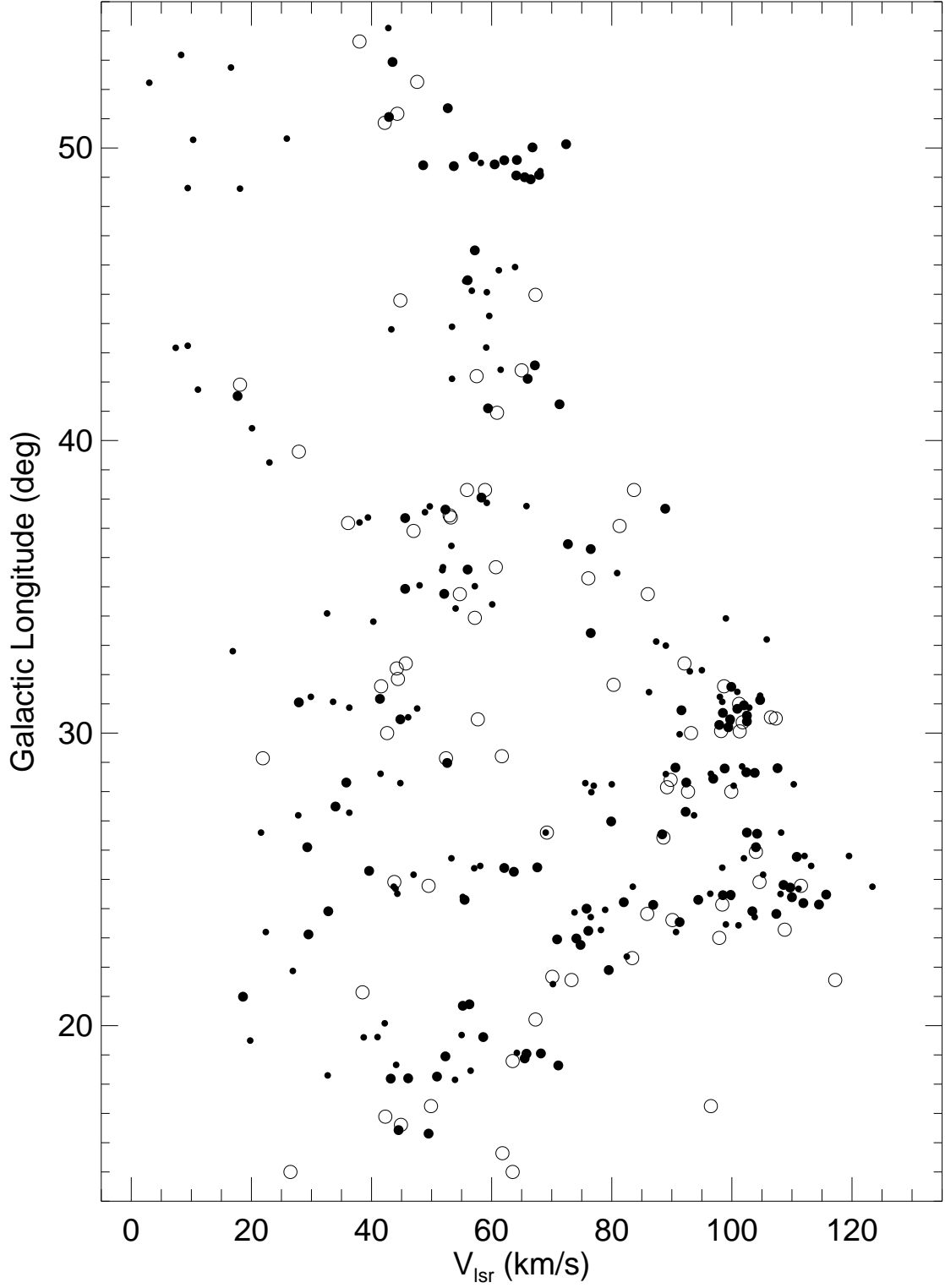


Fig. 1.— Longitude-LSR velocity diagram for H II regions located inside the GRS survey zone. The nebulae are shown projected onto the Galactic plane. The symbols represent UC nebulae (small filled circles), compact nebulae (medium filled circles), and diffuse nebulae (large open circles).

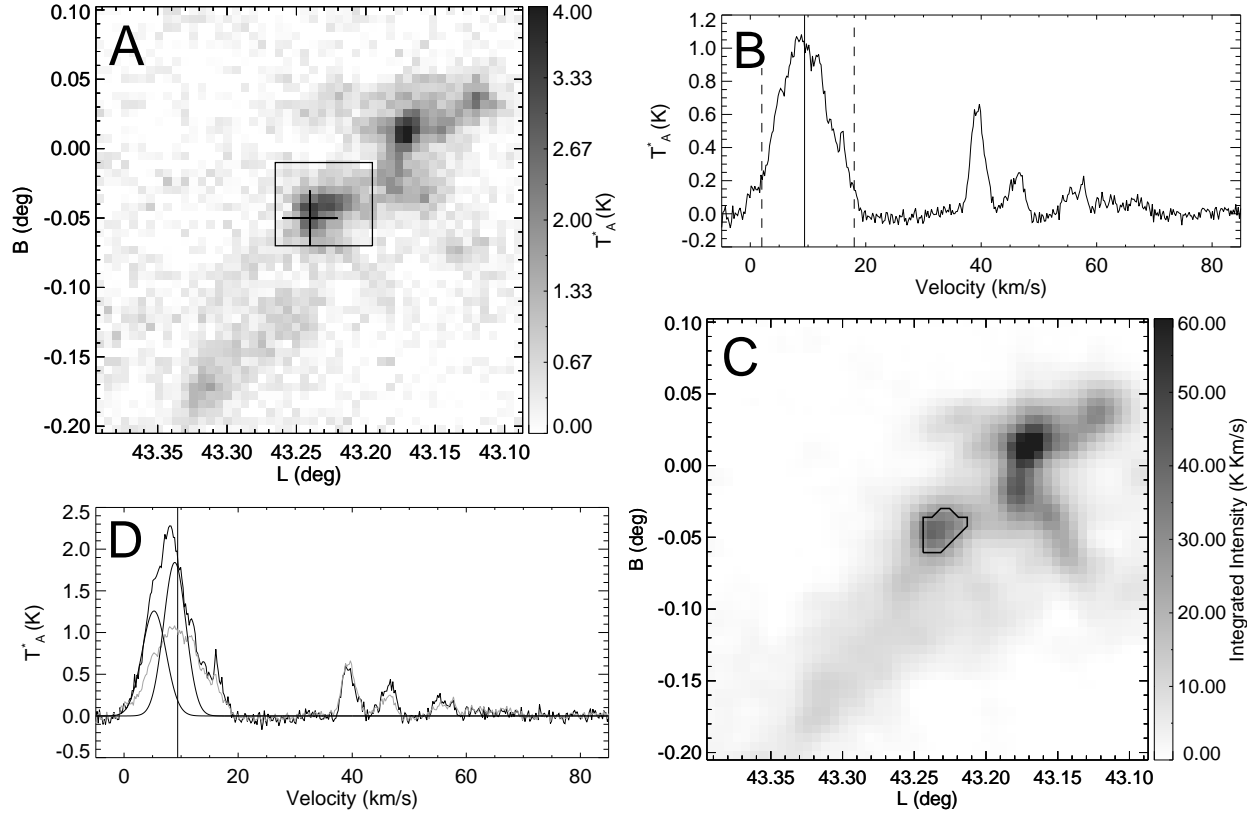


Fig. 2.— The CO/HII association procedure for the U43.24–0.05 H II region (see text). Panel A: Using single velocity channels near the RRL velocity and nominal H II region position we first locate the associated molecular emission. The black cross shows the H II region position. The black rectangle defines the extent of the ^{13}CO emission that is deemed to be associated with the H II region. Panel B: The average ^{13}CO spectrum of the GRS data cube voxels that lie within the panel A black rectangle is shown. The solid vertical line flags the H II region RRL velocity and the dashed lines show the velocity range of the associated emission. Panel C: The integrated intensity image made from the data cube using the line center velocity and FWHM line width found by the Panel B Gaussian fit is shown. This image is then used to define the final extent of ^{13}CO emission that is deemed to be associated with the H II region. The black outline shows this region which is defined by a threshold algorithm (see text). Panel D: The average ^{13}CO spectrum of the data cube voxels that lie within the panel C threshold defined region is shown. The vertical line flags the RRL velocity. The Gaussian fit to the emission line is used to derive the physical properties of the ^{13}CO gas associated with this H II region. The spectrum from panel B is shown in gray for comparison.

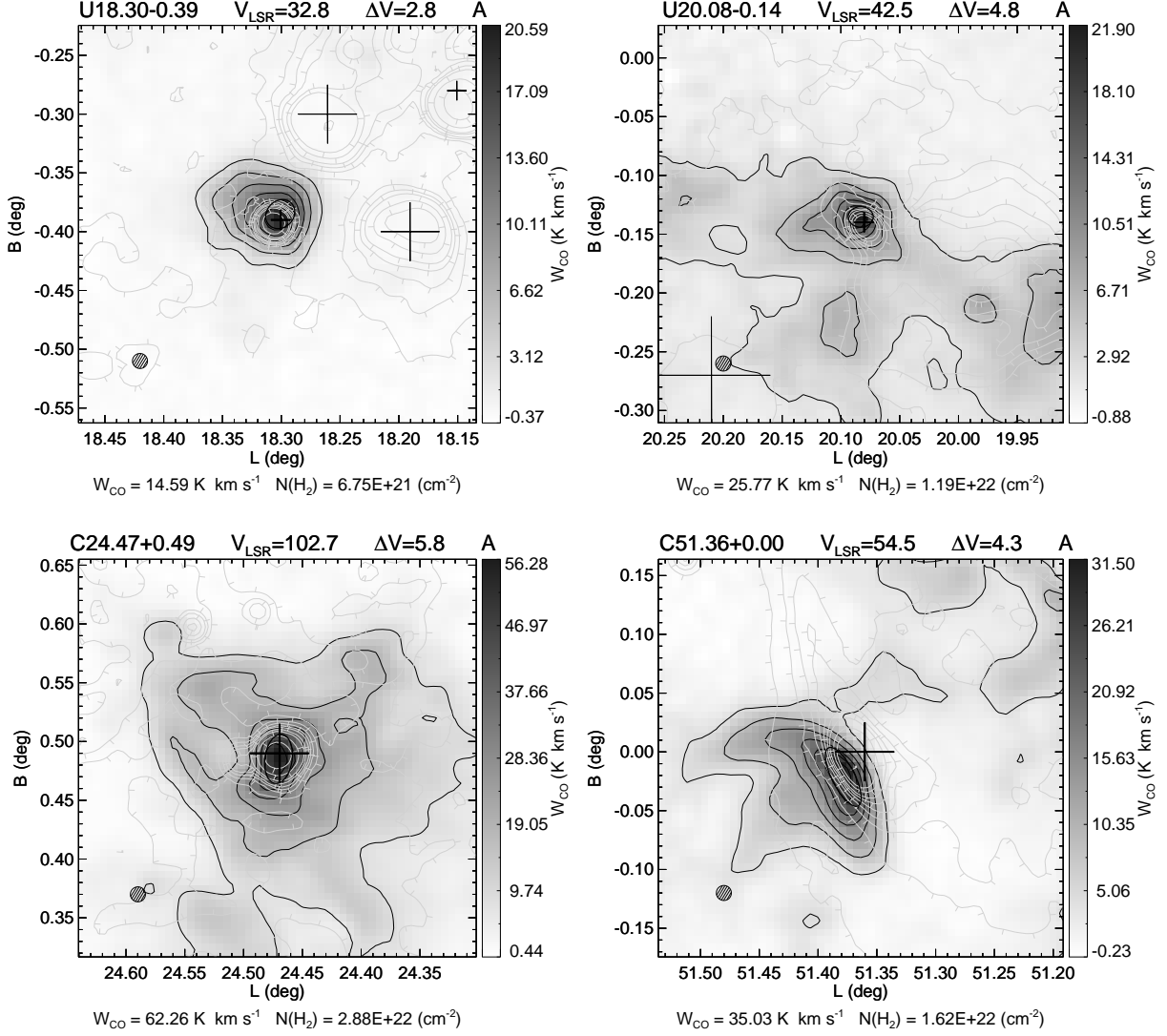


Fig. 3.— Integrated intensity images (grey scale and black contours) for a sample of H II regions with A confidence parameters. Nominal H II region positions are marked with crosses and our fitted ellipses are also shown. Contours of 21cm VGPS continuum emission are shown in grey. Tickmarks on the VGPS contours point downhill, towards decreasing values. See §5 for a detailed description of these images.

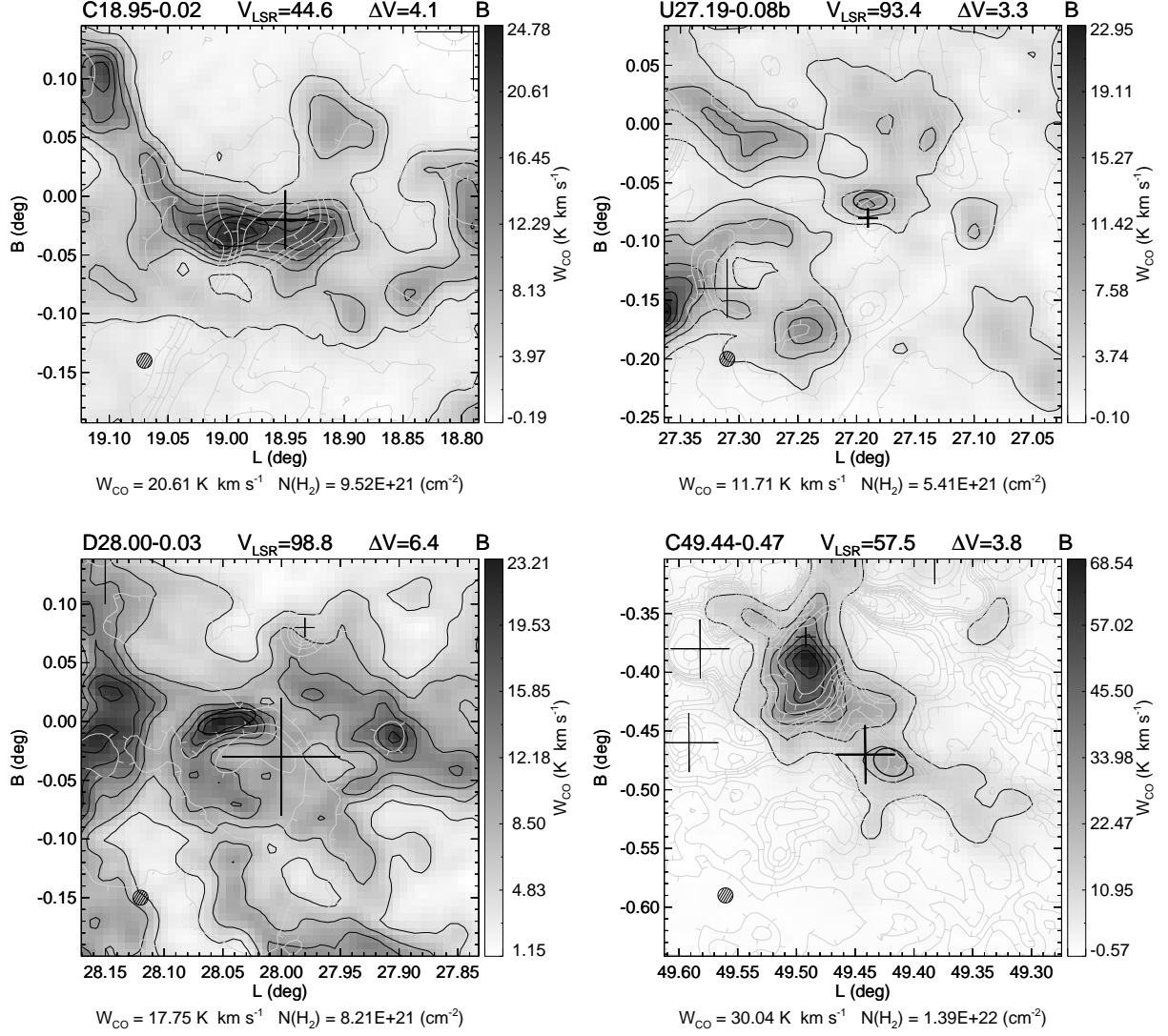


Fig. 4.— Integrated intensity images for a sample of H II regions with B confidence parameters. Other parameters are as in Figure 3.

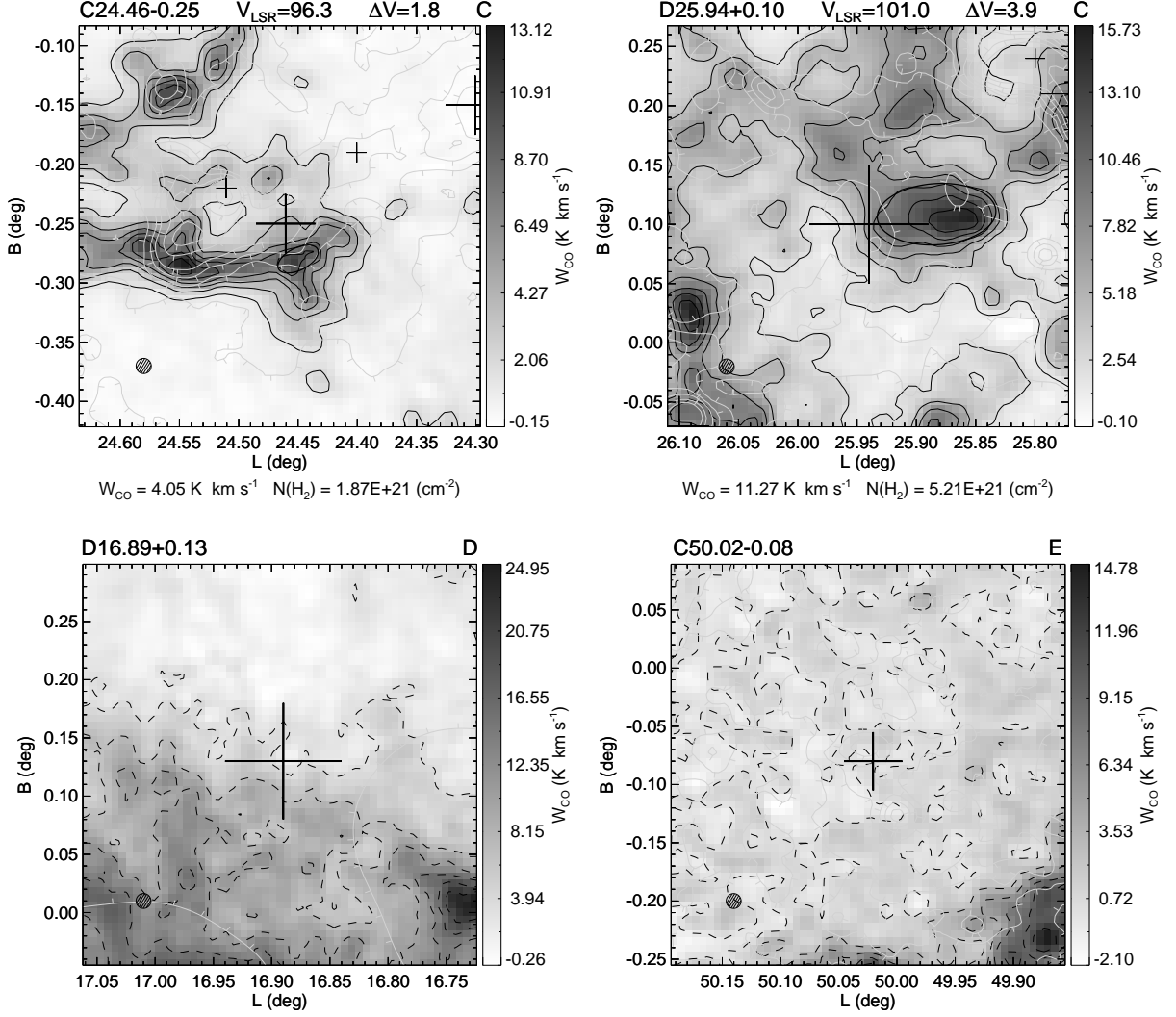


Fig. 5.— Integrated intensity images for a sample of H II regions with C confidence parameters (top row), D (lower left) and E (lower right). Fitted ellipses are shown for C sources only. Other parameters are as in Figure 3.

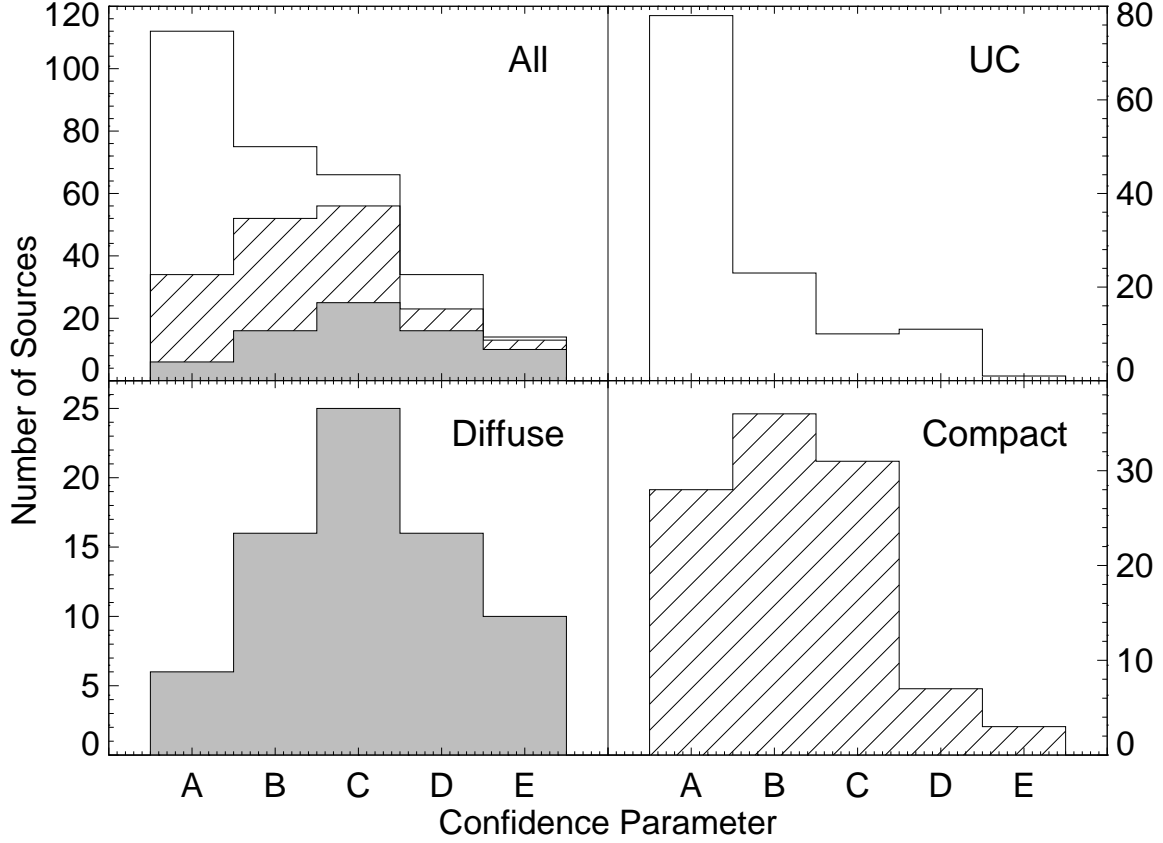


Fig. 6.— The number distributions of the qualitative confidence parameter, CP . Sources with associated molecular gas are rated A, B or C in order of decreasing confidence in the association (see §5 text). Confidence parameter D and E sources have little or no associated molecular emission, respectively. The top left panel is a stacked histogram where the top line shows the histogram for the entire sample of 301 H II regions. The open, hatched and grey histograms show the contribution that UC, Compact, and Diffuse nebulae, respectively, make to the total in each bin.

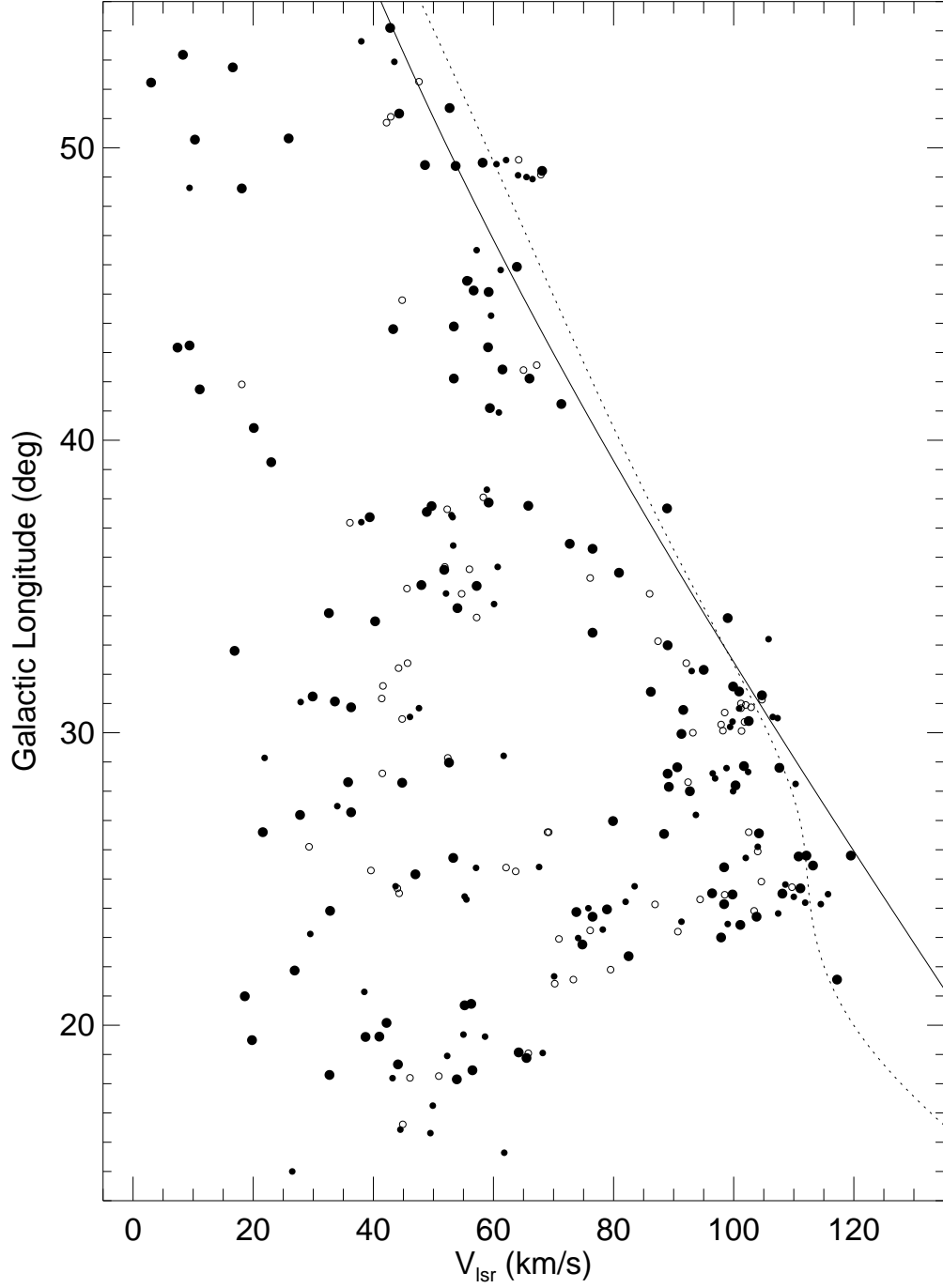


Fig. 7.— Longitude-LSR velocity diagram for 253 H II regions in our sample that show associated ^{13}CO emission. Symbols indicate the confidence parameter of each nebula: *CP* A (large filled circles), B (small filled circles), or C (small open circles). The lines show the loci of the LSR terminal velocity expected from two different Galactic rotation curve models: Clemens (1985) (dotted line) and Brand (1986) (full line).

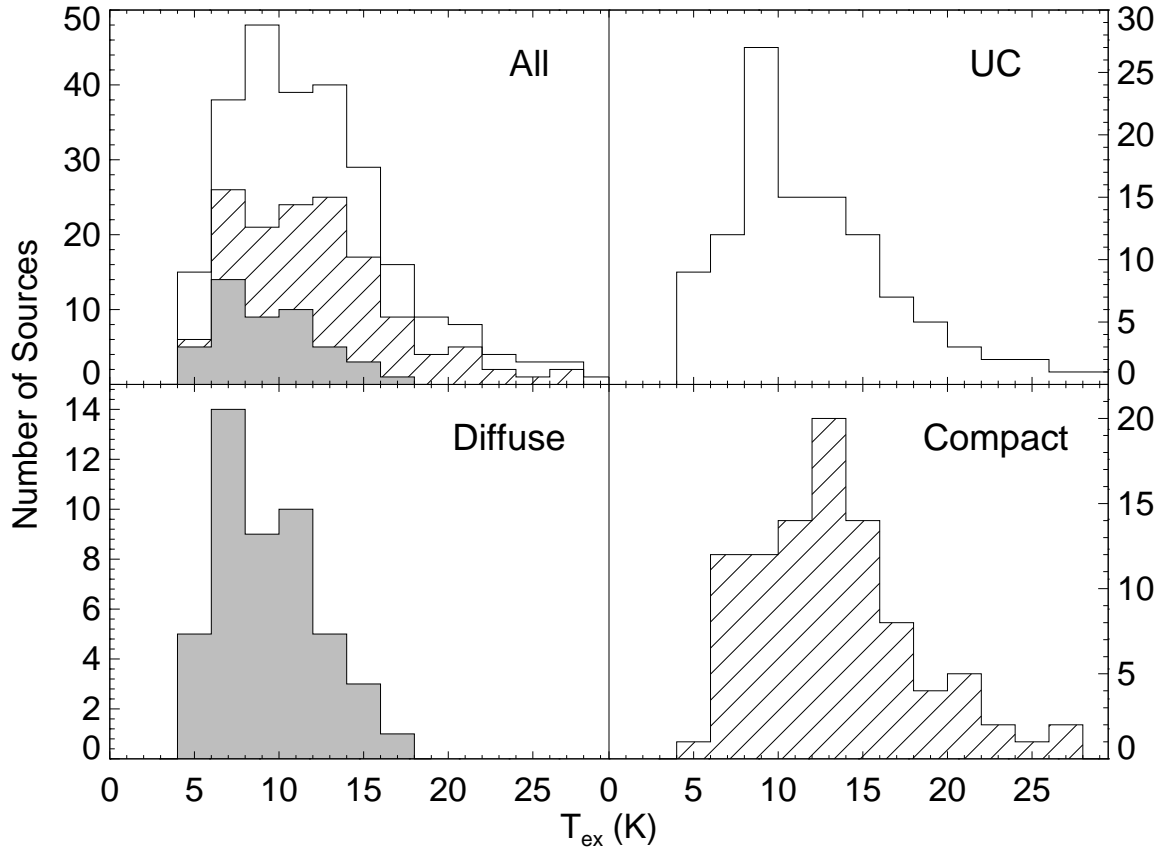


Fig. 8.— Nebular excitation temperature, T_{ex} , derived from the ^{12}CO survey of Sanders et al. (1986). Panels are the same as in Figure 6.

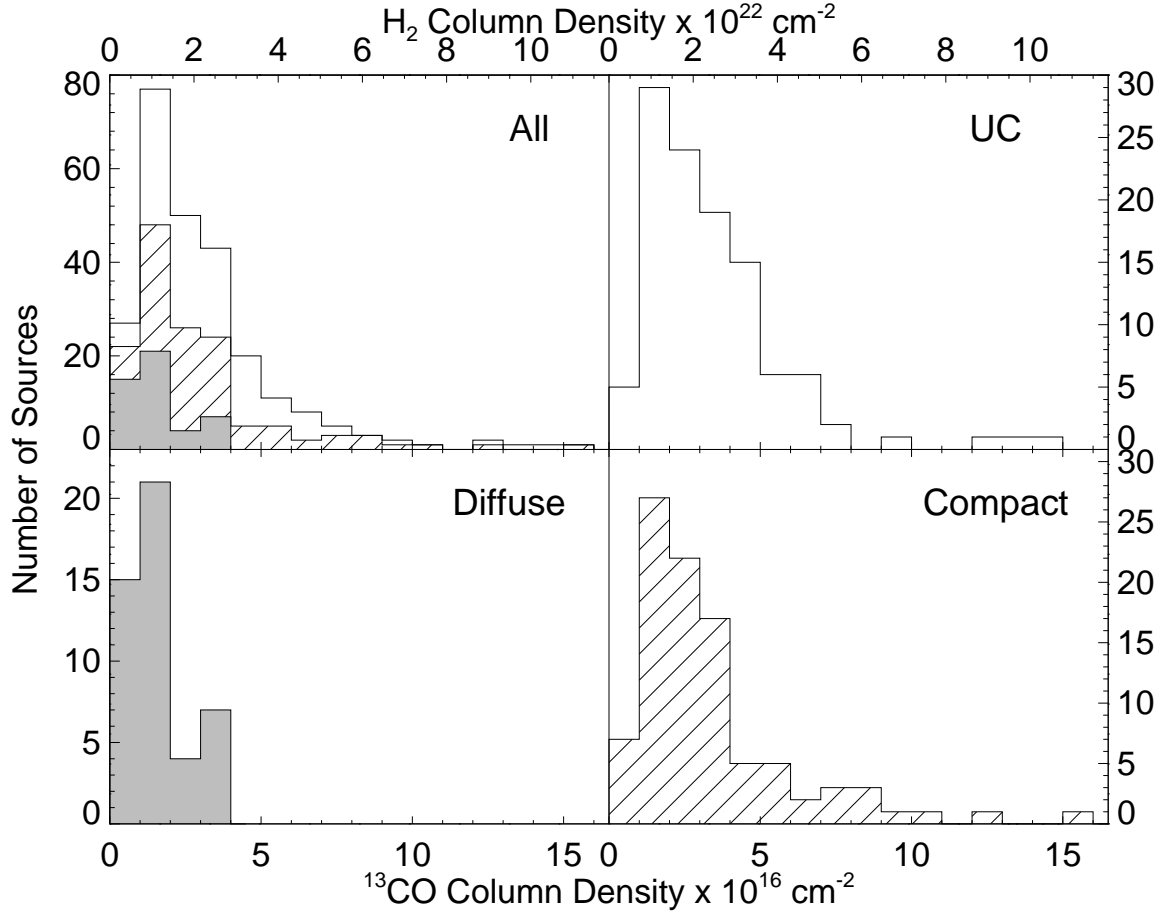


Fig. 9.— Estimated H_2 column density (top axis) and ^{13}CO column density (bottom axis) for the molecular clumps associated with our H II regions. Panels are the same as in Figure 6.

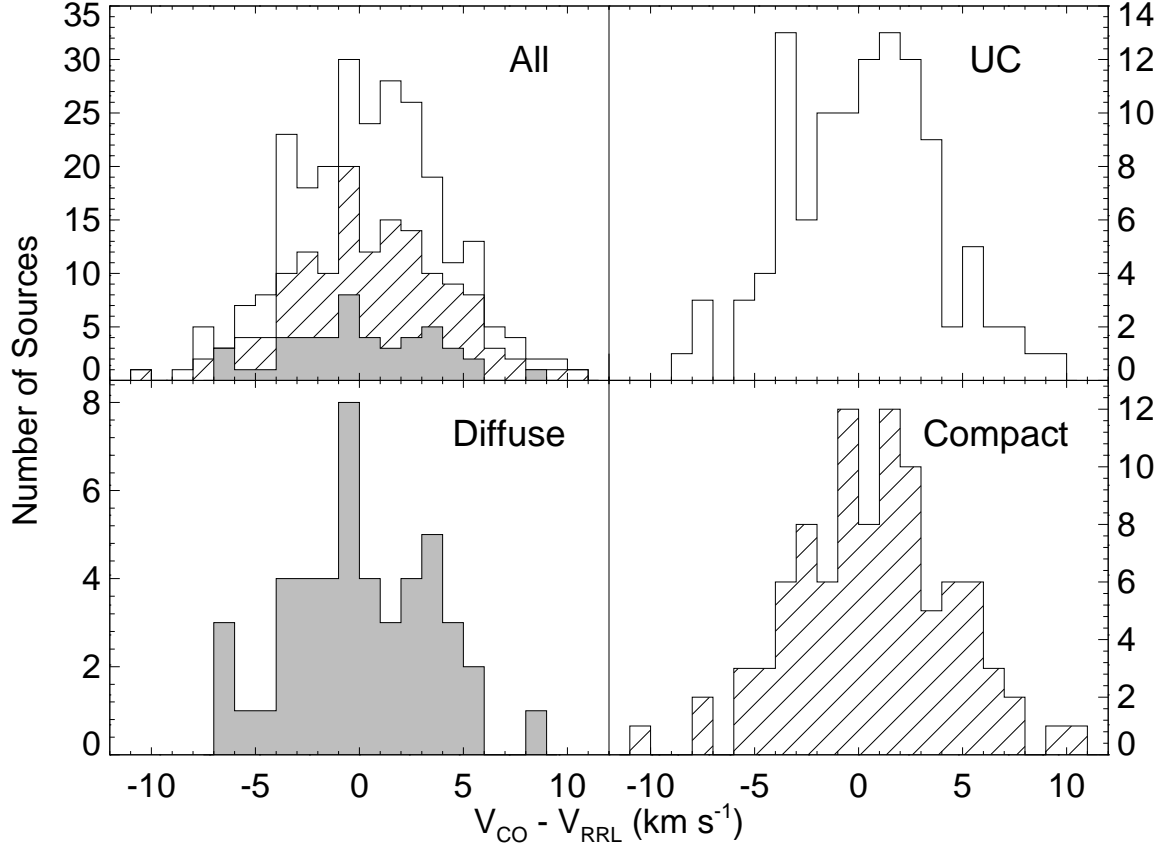


Fig. 10.— The LSR velocity difference between the H II region RRL and molecular gas ^{13}CO velocity. The distribution peaks near zero, as expected. Panels are the same as in Figure 6.

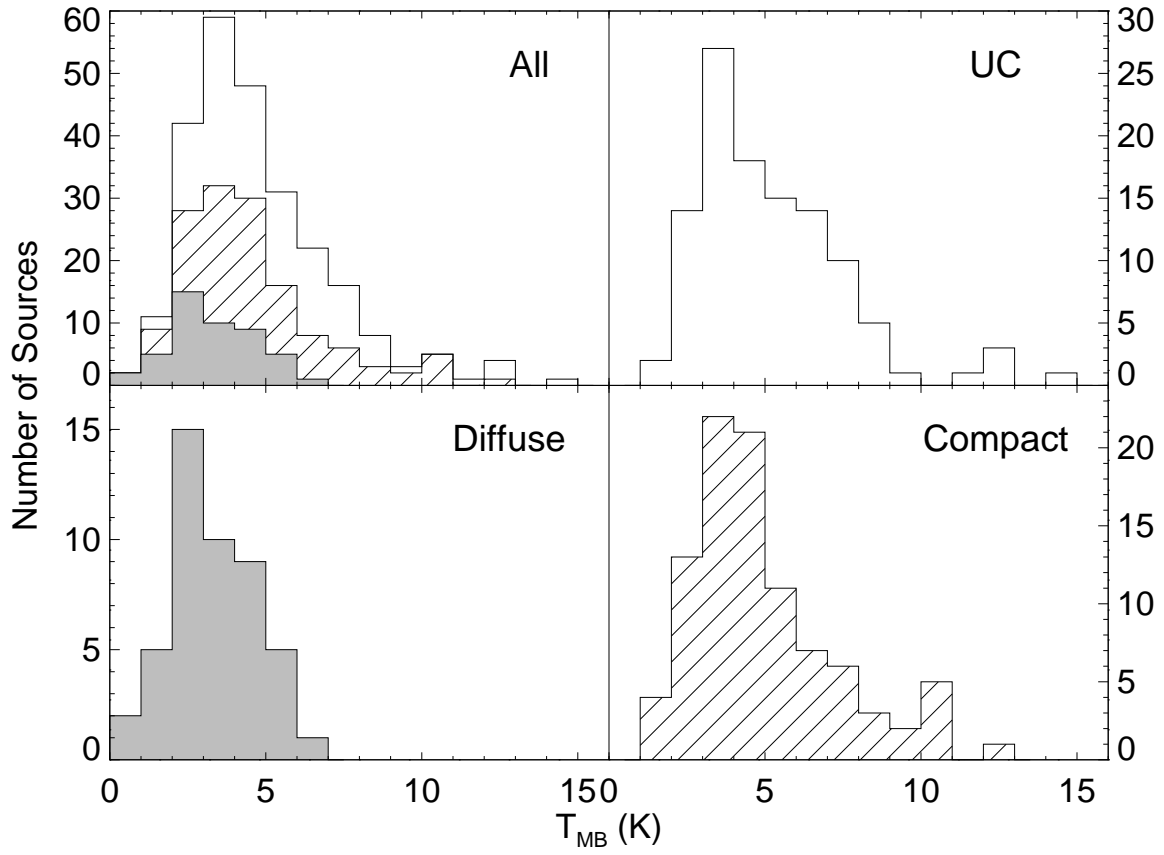


Fig. 11.— Main beam brightness temperature ^{13}CO line intensity from Gaussian fits. Panels are the same as in Figure 6.

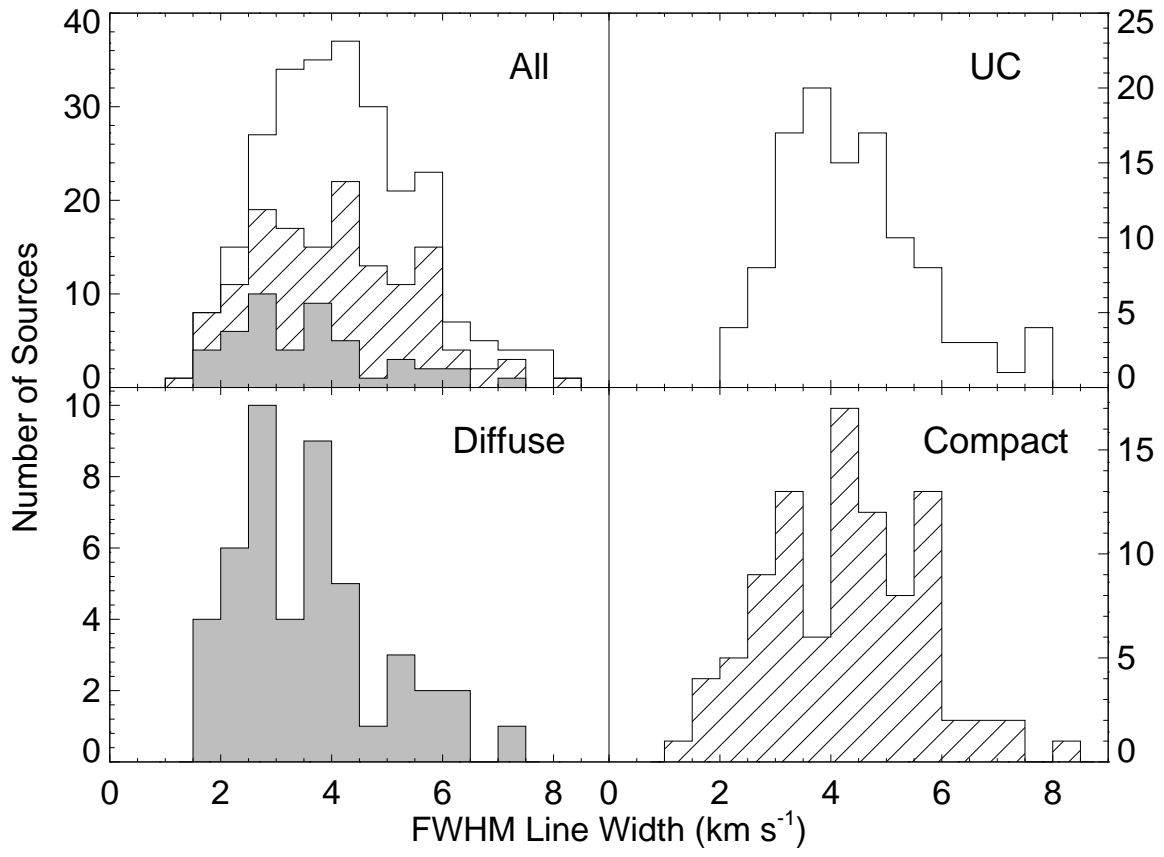


Fig. 12.— ^{13}CO FWHM line width from Gaussian fits. Panels are the same as in Figure 6.

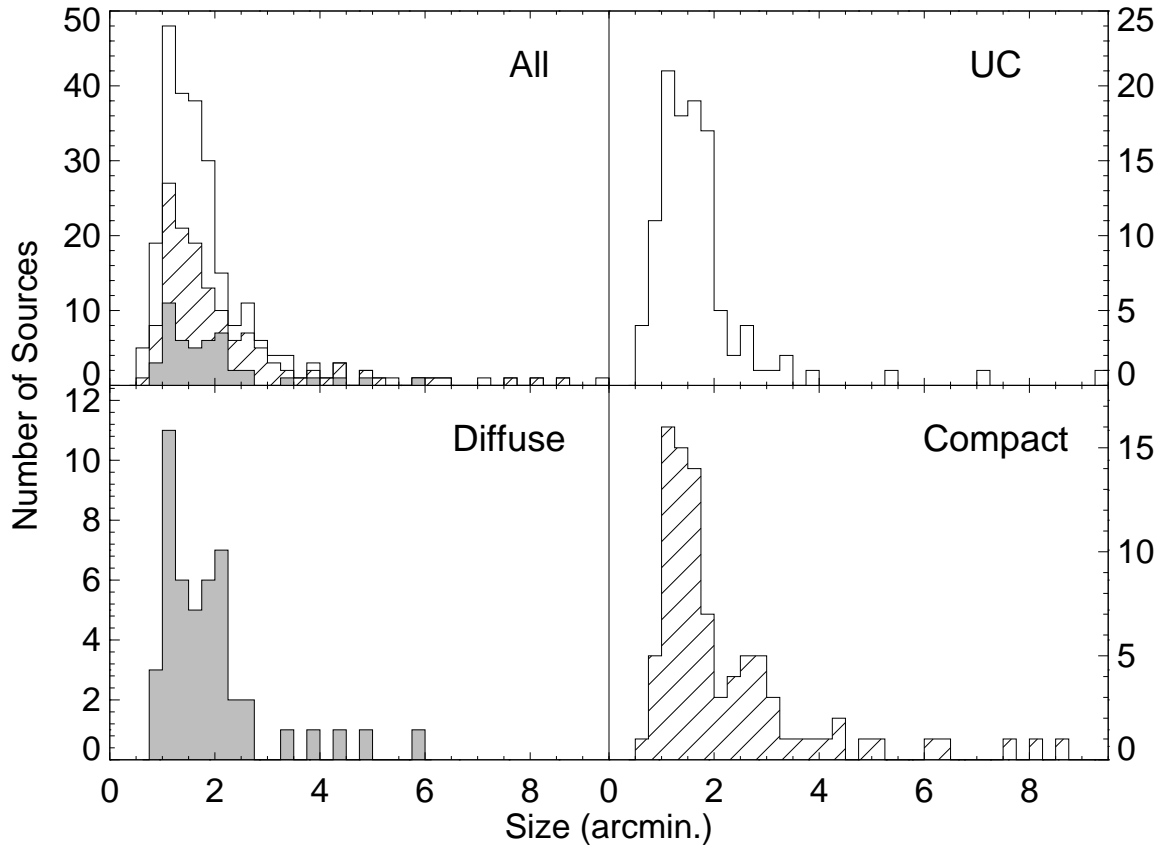


Fig. 13.— Angular size defined as the geometric mean diameter of the fitted ellipses. Panels are the same as in Figure 6.

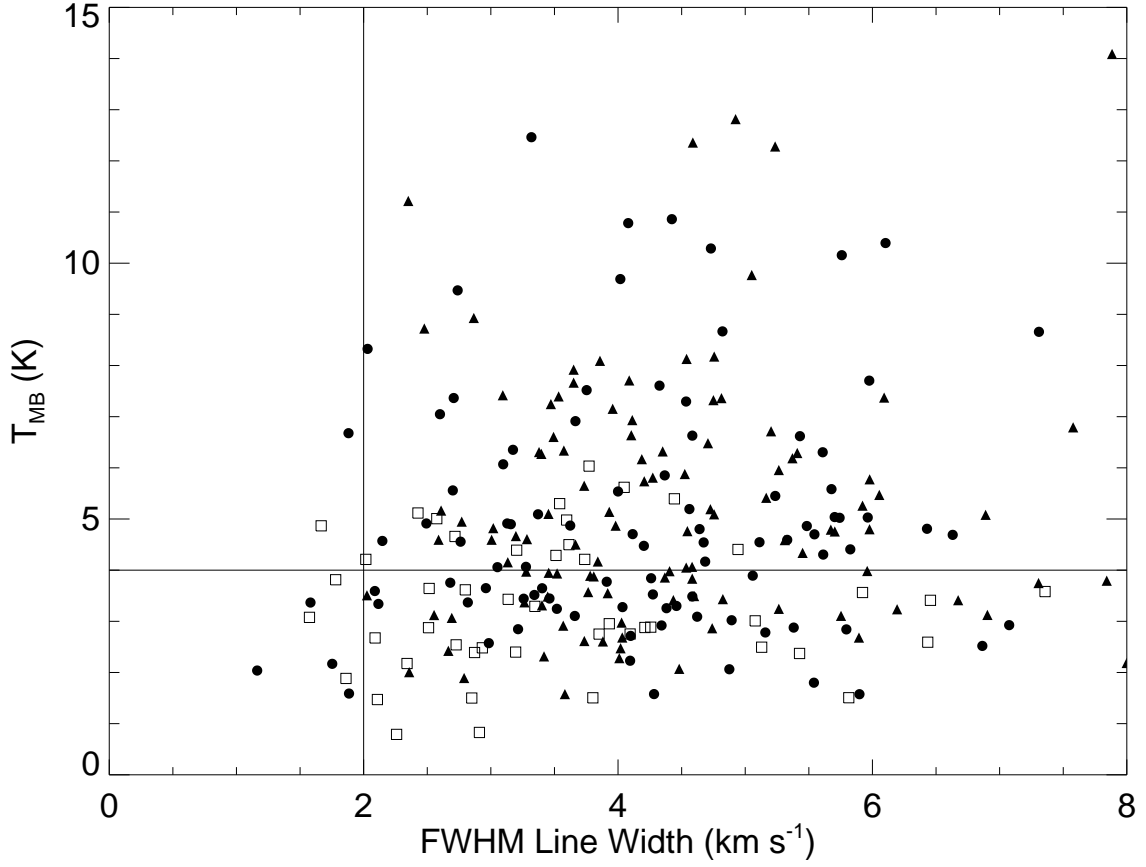


Fig. 14.— ^{13}CO line intensity plotted as a function of FWHM line width. Shown are all the *CP* A, B, or C sources: UC (filled triangles), Compact (filled circles), and Diffuse (open squares) nebulae. The lines dividing the figure into quadrants are from an analysis of molecular clumps in the GRS dataset (see §5.2).